


Cite this: *RSC Adv.*, 2023, 13, 28912

Exploration of the structural, vibrational, electronic, mechanical and thermal properties of $\text{Ru}_4\text{Al}_3\text{B}_2$ and $\text{Ru}_9\text{Al}_3\text{B}_8$: a DFT study

Arpon Chakraborty,^{ID a} M. N. H. Liton,^{ID ab} M. S. I. Sarker,^{ID *a} M. M. Rahman^a and M. K. R. Khan^{*a}

The structural, dynamical, electro-optical, mechanical, and thermal characteristics of the newly synthesized intermetallic compounds $\text{Ru}_4\text{Al}_3\text{B}_2$ and $\text{Ru}_9\text{Al}_3\text{B}_8$ have been studied under ambient and elevated pressure through density functional theory (DFT). The obtained lattice parameters of the compounds are consistent with the experimental values. The metallic character of these compounds is established by the band structure and density of states (DOS). The electronic charge density distribution and bond analysis imply that $\text{Ru}_4\text{Al}_3\text{B}_2$ and $\text{Ru}_9\text{Al}_3\text{B}_8$ have mainly both ionic and covalent bonding. The non-negative phonon dispersion frequency of the compounds reaffirms their dynamical stability. Both compounds are tough as well as have high melting points, and hence, can be applied in harsh conditions. Mechanical properties are significantly improved under pressure. Thermal barrier coating (TBC) is a possible field of application for both compounds. The different thermal properties such as the Debye temperature (θ_D), Grüneisen parameter (γ), melting temperature (T_m), minimum thermal conductivity (K_{\min}) and lattice thermal conductivity (κ_{ph}) of these compounds have been studied to figure out the suitable application areas in thermally demanding situations. The pressure and temperature dependent bulk modulus (B) and other thermodynamic properties have also been analyzed, which suggested that the present compounds are strong candidates for device applications at high temperature and pressure. Owing to their high optical absorptivity and reflectivity in the UV region, they are also candidates for UV-based applications. Furthermore, they also have applicability in the fields of electronics, aviation, energy storage, and supercapacitor devices for their superior electronic, thermal and mechanical properties.

Received 6th August 2023
Accepted 26th September 2023

DOI: 10.1039/d3ra05334b

rsc.li/rsc-advances

1. Introduction

The development of novel materials with extraordinary properties is an important field of study in condensed matter physics. The exploration of new phases of intermetallic compounds in recent years has resulted in the discovery of several fascinating materials such as Rh_3X ($\text{X} = \text{Ti}, \text{Zr}, \text{Hf}, \text{V}, \text{Nb}, \text{Ta}$), YbAl_3 , and TiFeH_2 .^{1–5} Several intermetallic compounds have an appealing combination of physical and mechanical qualities, such as a high melting point, low density, low porosity, and resistance to oxidation or corrosion. They are widely used in the aerospace sector, aircraft and automobile engines, biomedical instruments, microprocessors, electronics, batteries, hydrogen storage systems, and chemical industries.⁶ At the interface of a solder joint in an electronic circuit, a layer comprising one or more intermetallic compounds inevitably forms between the solder and the relevant system.^{7–9}

Ru is a rare transition metal belonging to group VIII in the periodic table. It is one of the rarest elements in the earth's crust, having an abundance of only 0.001 ppm. Unlike the lighter congener Fe, Ru is paramagnetic at room temperature. Ruthenium is highly resistant to corrosion and oxidation. While ruthenium is not one of the most heavily studied materials, it has been the subject of significant research in recent years. The unique properties of ruthenium-based compounds make them attractive for a wide range of applications such as catalysis, electronics, energy storage and conversion, turbines of jet engines, supercapacitors, biomedical sectors like biomedicines, *etc.*^{10–16} Ru and its complexes are mostly utilized in the measurement of ferritin, calcitonin, cyclosporine, and folate levels in the human body for medical diagnosis.¹⁷ Ru-based compounds have also been used in cancer treatment, as they have been found to be effective at killing cancer cells while leaving healthy cells intact.^{18–21} So, there are a lot of possibilities to explore the compounds in these types of applications.

Recently, Hirt *et al.*²² synthesized two new Ru-based ternary borides, $\text{Ru}_4\text{Al}_3\text{B}_2$ and $\text{Ru}_9\text{Al}_3\text{B}_8$. They prepared single crystals of $\text{Ru}_4\text{Al}_3\text{B}_2$ and $\text{Ru}_9\text{Al}_3\text{B}_8$ by using the arc melting method. X-ray

^aDepartment of Physics, University of Rajshahi, Rajshahi-6205, Bangladesh. E-mail: mfkhrkhan@yahoo.com; samiul-phy@ru.ac.bd

^bDepartment of Physics, Begum Rokeya University, Rangpur-5400, Bangladesh


Diffraction (XRD) showed that $\text{Ru}_9\text{Al}_3\text{B}_8$ has a hexagonal structure whereas $\text{Ru}_4\text{Al}_3\text{B}_2$ has a tetragonal shape. Since both $\text{Ru}_4\text{Al}_3\text{B}_2$ and $\text{Ru}_9\text{Al}_3\text{B}_8$ are fairly new compounds, there is much room to investigate their different physical properties to find the possible area of technological applications.

In this study, we have emphasized on exploring the ground state structural, vibrational, electronic, mechanical, optical, and thermal properties of the newly synthesized $\text{Ru}_4\text{Al}_3\text{B}_2$ and $\text{Ru}_9\text{Al}_3\text{B}_8$, under ambient and elevated pressure in the framework of DFT for the first time. Overall, this study is an essential step toward a better understanding of the characteristics of the compounds, highlighting their potential for future technological applications. The findings given here are a useful resource for the scientific community, opening up new options for future research on this intriguing topic.

2. Computational method

Ab initio technique was used for the exploration of the ground state properties of the metallic $\text{Ru}_4\text{Al}_3\text{B}_2$ and $\text{Ru}_9\text{Al}_3\text{B}_8$ compounds by employing the Kohn–Sham density functional theory.²³ Cambridge Serial Total Energy Package (CASTEP) code was used for the detailed calculations.²⁴ For the purpose of structural optimization of the compounds, we selected the generalized gradient approximation within the Perdew–Burke–Ernzerhof (GGA-PBE) functional.²⁵ To model the electron–ion interactions, Vanderbilt-type ultra-soft pseudopotential was used.²⁵ The BFGS²⁶ technique, which stands for Broyden–Fletcher–Goldfarb–Shanno, has been used to optimize the atomic configuration. To perform the pseudo atomic computations, the valence electron configurations of Ru, Al, and B atoms have been considered as $[5s^1 4p^6 4d^7]$, $[3s^2 3p^1]$, and $[2s^2 2p^1]$, respectively. For the compounds involved in the plane wave expansion process, a kinetic energy cut-off of 550 eV was used. During the optimization process, the following additional parameters were used: k -point for Brillouin zone (BZ) sampling of $4 \times 4 \times 12$ and $4 \times 4 \times 11$ special points in Monkhorst–Pack grid scheme for $\text{Ru}_4\text{Al}_3\text{B}_2$ and $\text{Ru}_9\text{Al}_3\text{B}_8$, respectively; energy convergence thresholds of 5×10^{-6} eV per atom; maximum force of $0.01 \text{ eV } \text{\AA}^{-1}$; maximum stress of 0.02 GPa and maximum displacement of $5 \times 10^{-4} \text{ \AA}$. The phonon dispersion (PDC) and phonon density of states (PHDOS) were calculated following the finite displacement supercell method.²⁷ A supercell with a volume two and three times that of the unit cell of $\text{Ru}_4\text{Al}_3\text{B}_2$ and $\text{Ru}_9\text{Al}_3\text{B}_8$, respectively, comes from a supercell with a fixed supercell dimension and a cutoff radius of 3.0. For phonon calculation, cut-off energy of 300 eV was used for both compounds.

The direct explanation of many solid-state phenomena depends critically on the thermal characteristics of crystalline materials. At various temperatures and pressures, the bulk moduli, Debye temperatures, specific heats, volume thermal expansion coefficients, entropies, and internal energies of the compounds have been assessed. Baroni developed a formula to identify the temperature dependence of the energy as:²⁷

$$E(T) = E_{\text{tot}} + E_{\text{zp}} + \int \frac{\hbar\omega}{\exp\left(\frac{\hbar\omega}{kT}\right) - 1} F(\omega) d\omega$$

where E_{zp} is defined as the zero-point vibrational energy, k is Boltzmann's constant, \hbar is reduced Planck's constant, and $F(\omega)$ is the phonon density of states. E_{zp} can be estimated as:

$$E_{\text{zp}} = \frac{1}{2} \int F(\omega) \hbar\omega d\omega$$

F is the vibrational contribution to the free energy and it is:

$$F(T) = E_{\text{tot}} + E_{\text{zp}} + kT \int F(\omega) \ln \left[1 - \exp\left(-\frac{\hbar\omega}{kT}\right) \right] d\omega$$

S is defined as the vibrational contribution to the entropy and it can be written as:

$$S(T) = k \left\{ \int \frac{\frac{\hbar\omega}{kT}}{\exp\left(\frac{\hbar\omega}{kT}\right) - 1} F(\omega) d\omega - \int F(\omega) \ln \left[1 - \exp\left(-\frac{\hbar\omega}{kT}\right) \right] d\omega \right\}$$

And the lattice contribution to the heat capacity, C_V , is:

$$C_V(T) = k \int \frac{\left(\frac{\hbar\omega}{kT}\right)^2 \exp\left(\frac{\hbar\omega}{kT}\right)}{\left[\exp\left(\frac{\hbar\omega}{kT}\right) - 1\right]^2} F(\omega) d\omega$$

The actual heat capacity which can be compared to that predicted by the Debye model is a popular portrayal of experimental data on heat capacity. This gives rise to the temperature-dependent Debye temperature, $\Theta_D(T)$. In the Debye model, heat capacity is given by:²⁸

$$C_V^D(T) = 9Nk \left(\frac{T}{\Theta_D}\right)^3 \int_0^{\Theta_D/T} \frac{x^4 e^x}{(e^x - 1)^2} dx$$

where N is the number of atoms per cell. Thus, the value of the Debye temperature, Θ_D , at a given temperature, T , is achieved by calculating the actual heat capacity and then inverting it to obtain Θ_D .

Specific heat at constant pressure (C_P) can be calculated by calculating the linear thermal expansion coefficient (TEC) first, by the following equations:

$$\text{TEC} = \frac{\gamma C_V}{3B_T V_m}$$

$$C_P = C_V [1 + (\text{TCE})\gamma T]$$

where, B_T , V_m , and γ are the isothermal bulk modulus, molar volume, and Grüneisen parameter, respectively.

We used the quasi-harmonic Debye model to evaluate the thermodynamic properties where the temperature range was



selected from 0 to 1000 K. The quasi-harmonic Debye model was described by Otero-de-La Roza *et al.*^{29,30} Utilizing the complex dielectric function, $\varepsilon(\omega) = \varepsilon_1(\omega) + i\varepsilon_2(\omega)$, the optical properties of $\text{Ru}_4\text{Al}_3\text{B}_2$ and $\text{Ru}_9\text{Al}_3\text{B}_8$ were studied in the ground state. Kramers–Kronig relationships, which use the response function, can be used to derive the real part $\varepsilon_1(\omega)$ of the dielectric function from the imaginary part $\varepsilon_2(\omega)$. The electrical band structure is used to determine the imaginary portion, $\varepsilon_2(\omega)$, using the following formula:³²

$$\varepsilon_2(\omega) = \frac{2e^2\pi}{\Omega\varepsilon_0} \sum_{k,v,c} k \Psi_k^c |\hat{u} \hat{r} \Psi_k^v|^2 \delta(E_k^c - E_k^v - E)$$

In this equation, Ω is the volume of the unit cell, ω is the frequency of the incident electromagnetic wave (photon), e is the electronic charge, and Ψ_k^c and Ψ_k^v are the conduction and valence band wave functions at a given wave vector k , respectively. During the photon-induced transfer of the electron from the valence to the conduction band, the delta function ensures energy and momentum conservation. The standard relations^{33,34} can be used to determine the additional optical parameters such as the absorption coefficient, refractive index, reflectivity, photo-conductivity, and energy loss function when the energy dependent dielectric function $\varepsilon(\omega)$ is known.

3. Results and discussion

3.1 Structural properties

The two bi-metallic borides have different structures. $\text{Ru}_4\text{Al}_3\text{B}_2$ has a tetragonal structure with space group $P4/mmm$ while $\text{Ru}_9\text{Al}_3\text{B}_8$ has a hexagonal form belonging to the space group $P6_3/m$,²² which are depicted in Fig. 1. The Wyckoff positions of the atoms are reported in ref. 22. Table 1 provides a list of the available experimental data as well as the optimized lattice parameters at zero pressure. In terms of volume V_0 , the obtained findings using the functional GGA-PBE diverge from the experimental values by less than 0.95% for $\text{Ru}_4\text{Al}_3\text{B}_2$ and 2.37% for $\text{Ru}_9\text{Al}_3\text{B}_8$. Therefore, the obtained results possess excellent agreement with the experimental data. As the pressure increases, the lattice parameters become smaller, and as a result, the volume shrinks. One interesting fact is that the

Table 1 Calculated lattice parameters ($a = b$ and c in Å) and volume (V in Å³) of $\text{Ru}_4\text{Al}_3\text{B}_2$ and $\text{Ru}_9\text{Al}_3\text{B}_8$ at 0 GPa

| Compound | This work | | | | Ref. 22 | | |
|------------------------------------|-----------|-------|-------|--------|---------|-------|--------|
| | a | c | a/c | V | a | c | V |
| $\text{Ru}_4\text{Al}_3\text{B}_2$ | 8.540 | 2.935 | 2.910 | 214.04 | 8.515 | 2.924 | 212.01 |
| $\text{Ru}_9\text{Al}_3\text{B}_8$ | 9.155 | 2.932 | 3.122 | 212.84 | 9.078 | 2.913 | 207.91 |

ratio a/c decreases with increasing pressure for both compounds. It indicates that the effect of pressure is superior in the a - (and b -) axis compared to the c -axis. After applying a pressure of 30 GPa, the decrease in volume is 9.98% for $\text{Ru}_4\text{Al}_3\text{B}_2$ as compared to 8.78% for $\text{Ru}_9\text{Al}_3\text{B}_8$, which means $\text{Ru}_4\text{Al}_3\text{B}_2$ is more prone to pressure compared to $\text{Ru}_9\text{Al}_3\text{B}_8$.

The structural stability of the two compounds can be confirmed by calculating the formation enthalpy of the respective compounds using the available relations.³¹ The formation enthalpies of the compounds under study were calculated by subtracting the energies of individual elements from the total energy using the following equation:

$$\Delta H_f(\text{Ru}_m\text{Al}_3\text{B}_n) = E_{\text{total}}(\text{Ru}_m\text{Al}_3\text{B}_n) - m \times E(\text{Ru}) - 3 \times E(\text{Al}) - n \times E(\text{B})$$

At $P = 0, 10, 20$ and 30 GPa, the calculated formation enthalpies were found to be $-7.525, -7.510, -7.474$ and -7.423 eV per atom for $\text{Ru}_4\text{Al}_3\text{B}_2$, and $-7.934, -7.922, -7.894$ and -7.853 eV per atom for $\text{Ru}_9\text{Al}_3\text{B}_8$, respectively, which indicates that they are energetically stable. However, the formation enthalpies decrease very slowly with increasing pressure, which may be a sign of opposing effect towards the stability of both compounds.

The normalized values of the lattice parameters (a/a_0 and c/c_0) are given in Fig. 2, together with the normalized and volumetric value of V/V_0 (inset). The optimized lattice parameters (a_0, c_0 , and V_0) and the volume at atmospheric pressure are given accordingly. As can be observed from Fig. 2, for both $\text{Ru}_4\text{Al}_3\text{B}_2$ and $\text{Ru}_9\text{Al}_3\text{B}_8$, each of the normalized values decreases

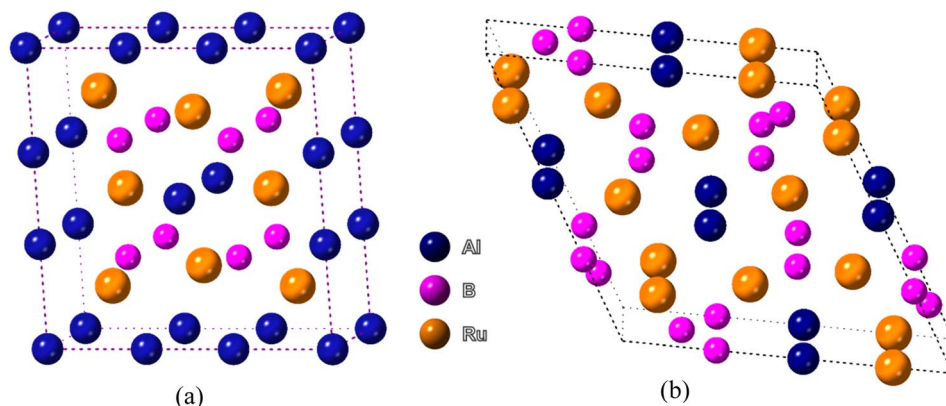


Fig. 1 Schematic 3D crystal structure of (a) $\text{Ru}_4\text{Al}_3\text{B}_2$, and (b) $\text{Ru}_9\text{Al}_3\text{B}_8$ compounds. The crystallographic directions are also shown.



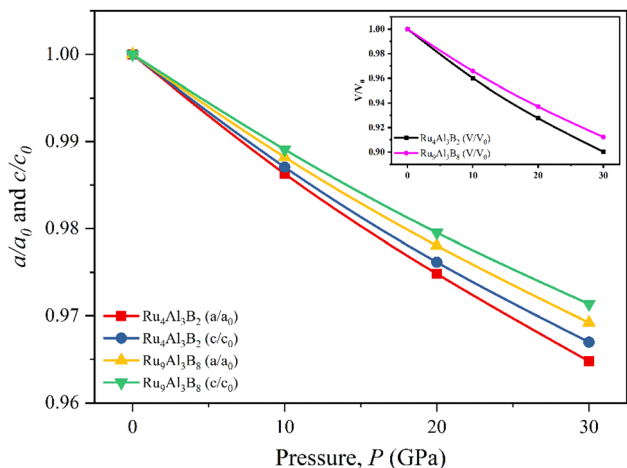


Fig. 2 Pressure dependent normalized lattice parameters, and volume (inset) of $\text{Ru}_4\text{Al}_3\text{B}_2$, and $\text{Ru}_9\text{Al}_3\text{B}_8$.

with increasing hydrostatic pressure. Additionally, for both compounds, the value of a/a_0 is lowered under applied pressure more quickly than that of c/c_0 , indicating that the a -axis is more contractible than the c -axis. One intriguing finding is that $\text{Ru}_4\text{Al}_3\text{B}_2$ has a greater reduction in lattice parameters than $\text{Ru}_9\text{Al}_3\text{B}_8$, indicating that the latter is more durable. Bond lengths and the material's internal degrees of freedom alter as a result of this decline in lattice parameters with higher pressure. The decline in lattice parameters from the zero pressure value may also be caused by density variations along crystallographic orientations.³²

3.2 Vibrational properties

Phonons play a crucial role in understanding the physical properties of materials such as thermal conductivity, thermal expansion, elastic properties, electrical conductivity, phase transitions, *etc.*^{33–35} It is necessary to test the dynamic stability of materials because they are often exposed to time-varying mechanical stresses. The dynamics of $\text{Ru}_4\text{Al}_3\text{B}_2$ and $\text{Ru}_9\text{Al}_3\text{B}_8$ based on their phonon dispersion curves (PDC) at zero

temperature and pressure have been analyzed by finite displacement supercell method.^{36,37} There are no negative frequencies found in the PDC (Fig. 3) of $\text{Ru}_4\text{Al}_3\text{B}_2$ and $\text{Ru}_9\text{Al}_3\text{B}_8$ in the whole BZ, indicating their dynamical stability. For $\text{Ru}_4\text{Al}_3\text{B}_2$, PDC consists of 54 phonon branches including 3 acoustic modes and 51 optical modes whereas, for $\text{Ru}_9\text{Al}_3\text{B}_8$, there are 60 phonon branches consisting of 3 acoustic modes and 57 optical modes. Acoustic modes (indicated by blue color) resulting from coherent vibrations of atoms outside their equilibrium positions are represented by the lower part of the phonon spectrum and the upper parts correspond to optical modes (indicated by red color). At Γ -point, the acoustic modes have zero frequency for both of the compounds, which is also an indication of their dynamical stability. Furthermore, acoustic and optical modes cross each other and no gap between these two. The overlapping between these two modes enhances their frequent interactions which provide more phonon scattering. This will in turn associated with the increasing anharmonicity which suppresses the thermal conductivity and hence increases the figure of merit (ZT).³⁸ Therefore, the thermoelectric performance (TE) is enhanced due to the overlap of the acoustic and optical modes.

3.3 Electronic properties

Electronic band structures for the optimized crystal structure of $\text{Ru}_4\text{Al}_3\text{B}_2$ and $\text{Ru}_9\text{Al}_3\text{B}_8$ are evaluated along the directions of high symmetry ($Z\text{-A-M-}\Gamma\text{-Z-R-X-}\Gamma$) and ($\Gamma\text{-A-H-K-}\Gamma\text{-M-L-H}$), respectively in the first Brillouin zone (BZ) at different pressures. The horizontal broken line indicates the Fermi level, E_F . The band structures of the compounds are shown in Fig. 4 and 5. As we can see, a number of bands (green color) cross the E_F for both compounds which indicates their metallic character. The effect of pressure on band structure is minimal on both compounds. Moreover, the dispersion of bands over all the regions in the Brillouin zone is quite similar. So, the effective mass and mobility of electrons do not vary largely.

Fig. 6 shows the computed total and partial density of states (TDOS and PDOS, respectively) of $\text{Ru}_4\text{Al}_3\text{B}_2$ and $\text{Ru}_9\text{Al}_3\text{B}_8$ as a function of energy. The E_F is indicated by the vertical dashed line. The properties of bonding and hybridization between

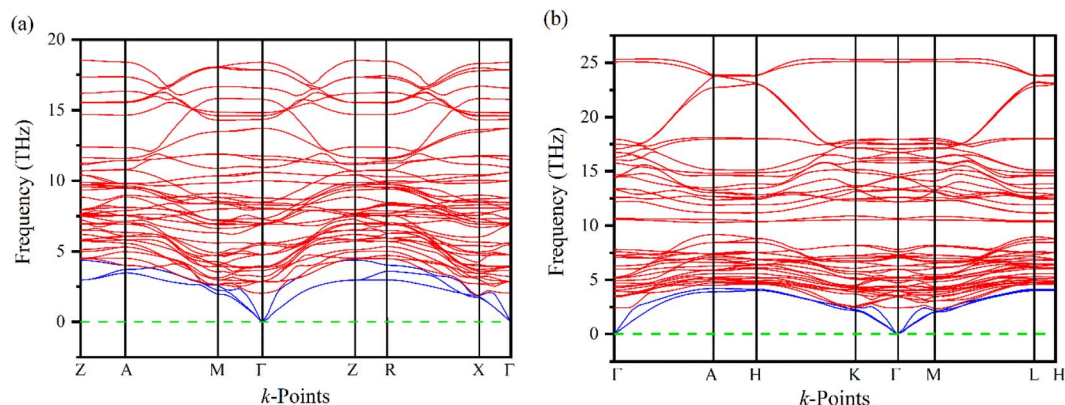


Fig. 3 Phonon dispersion curves (PDC) of (a) $\text{Ru}_4\text{Al}_3\text{B}_2$, and (b) $\text{Ru}_9\text{Al}_3\text{B}_8$.



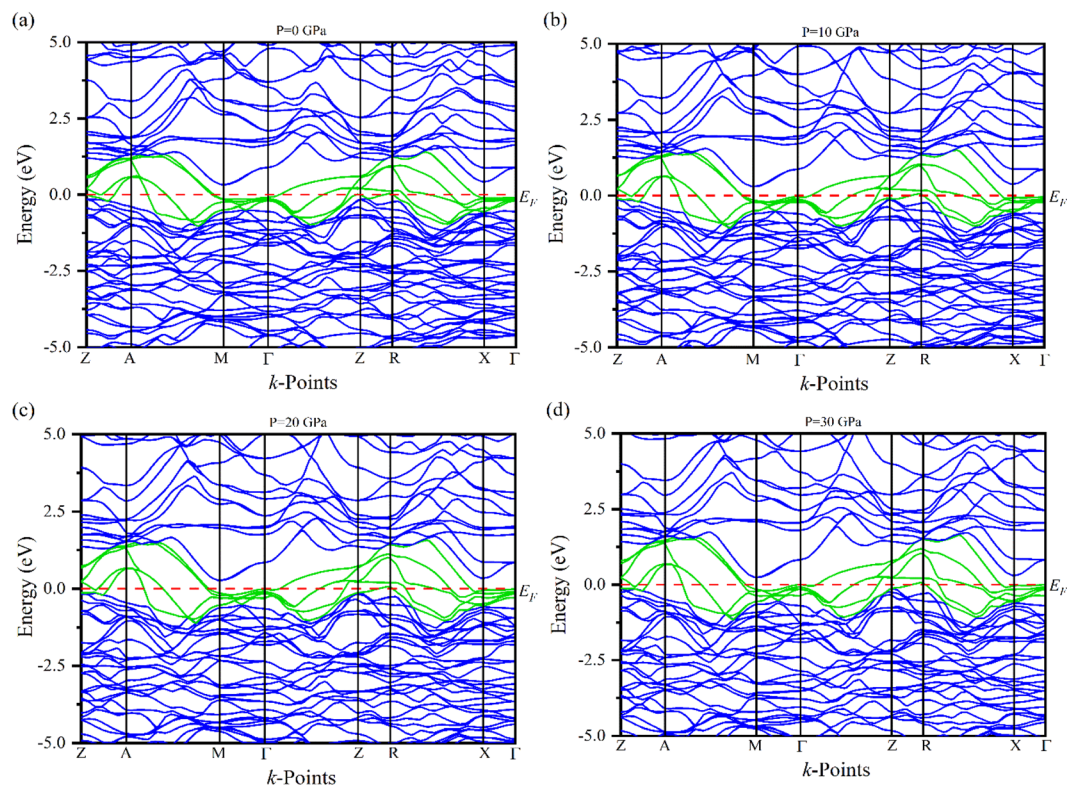


Fig. 4 The electronic band structures of $\text{Ru}_4\text{Al}_3\text{B}_2$ at (a) 0 GPa, (b) 10 GPa, (c) 20 GPa and (d) 30 GPa along the high symmetry directions.

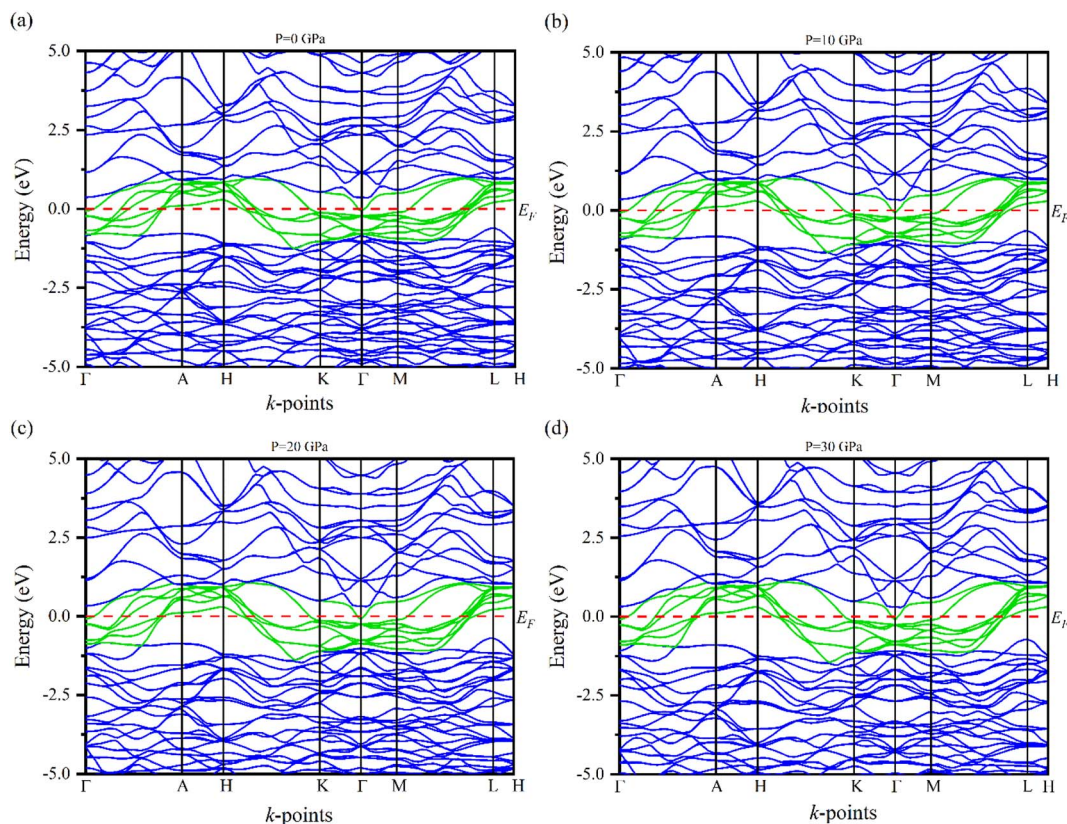


Fig. 5 The electronic band structures of $\text{Ru}_9\text{Al}_3\text{B}_8$ at (a) 0 GPa, (b) 10 GPa, (c) 20 GPa and (d) 30 GPa along the high symmetry directions.



different states can also be described by PDOS. The finite value of total DOS at the E_F supports the metallic character of both $\text{Ru}_4\text{Al}_3\text{B}_2$ and $\text{Ru}_9\text{Al}_3\text{B}_8$ compounds. From Fig. 6(a) and (b), the calculated value of TDOS ($N(E_F)$) at the Fermi level at zero pressure are 5.51 and 7.76 per eV per unit cell for $\text{Ru}_4\text{Al}_3\text{B}_2$ and $\text{Ru}_9\text{Al}_3\text{B}_8$, respectively, indicating that $\text{Ru}_9\text{Al}_3\text{B}_8$ show higher electrical conductivity than that of $\text{Ru}_4\text{Al}_3\text{B}_2$. The value of ($N(E_F)$) at E_F also determines the electronic stability of the compound.³² According to this, $\text{Ru}_4\text{Al}_3\text{B}_2$ is highly stable than $\text{Ru}_9\text{Al}_3\text{B}_8$. Near the E_F , the contribution on TDOSs comes from Ru-4d mainly, with nominal contribution from Al-3p and B-2p orbitals for both compounds. Thus, these orbitals have a dominating effect on the electrical conductivity of the compounds. The lowest valence bands in $\text{Ru}_4\text{Al}_3\text{B}_2$ are found to be created by the 2s orbital of B atom combined modestly with the Ru atom's 4d orbital in the energy range from -10.0 to -7.5 eV. Due to the significant hybridization between the Ru-4d, Al-3p, and B-2p orbitals, the TDOS of both $\text{Ru}_4\text{Al}_3\text{B}_2$ and $\text{Ru}_9\text{Al}_3\text{B}_8$ emerges from -5 eV to Fermi level. The hybridization between Al-3p and B-2p orbitals is mainly responsible for TDOS in the upper conduction band. According to the crystal field theory, the d-orbital is split into t_{2g} (d_{xy} , d_{yz} , d_{zx}) and e_g (d_{z^2} , $d_{x^2-y^2}$) states. The Ru has 7 valence electrons, where d_{xy} , d_{yz} states are fully occupied while d_{zx} , d_{z^2} , $d_{x^2-y^2}$ are half filled. More precisely, these half-filled states are hybridized with Al-p_x, and B-p_x, which are mainly responsible for the formation of the CB and VB, respectively.

In order to better understand the electrical properties of $\text{Ru}_4\text{Al}_3\text{B}_2$ and $\text{Ru}_9\text{Al}_3\text{B}_8$, we also examined the TDOS of these materials under various pressures. The effect of pressure on TDOS for both compounds is shown in Fig. 7. The position of the peaks shifts towards lower energy in the valence band and higher energy in the conduction band. The symmetry of the most prominent peak remains intact despite applying pressure for $\text{Ru}_4\text{Al}_3\text{B}_2$. The prominent peak appears at -4.2 eV for $\text{Ru}_9\text{Al}_3\text{B}_8$ and shifts towards lower energy with pressure. By applying pressure, the value of TDOS becomes smaller which indicates that the stability of the compounds increases with pressure.

In a normal metal or semiconductor, the DOS is typically a smooth, continuous function of energy. However, in some materials, the DOS exhibits a so-called "pseudogap", which is a region of reduced DOS at a certain energy range. The E_F for both $\text{Ru}_4\text{Al}_3\text{B}_2$ and $\text{Ru}_9\text{Al}_3\text{B}_8$ is located at the left of the pseudogap, or in the bonding region. Furthermore, the covalent bonding is present in the crystals since the position of pseudogap is very close to the E_F and this also notifies that the materials are highly stable and the mechanical strength of the compounds is very high.

The Fermi surface configuration determines the electrical and thermal properties of a material. In this context, we have constructed the Fermi surfaces of $\text{Ru}_4\text{Al}_3\text{B}_2$ and $\text{Ru}_9\text{Al}_3\text{B}_8$ compounds from the respective electronic band structures, as shown in Fig. 8. The Fermi surface structure of the $\text{Ru}_4\text{Al}_3\text{B}_2$ is quite different from that of the $\text{Ru}_9\text{Al}_3\text{B}_8$. For $\text{Ru}_4\text{Al}_3\text{B}_2$, there is

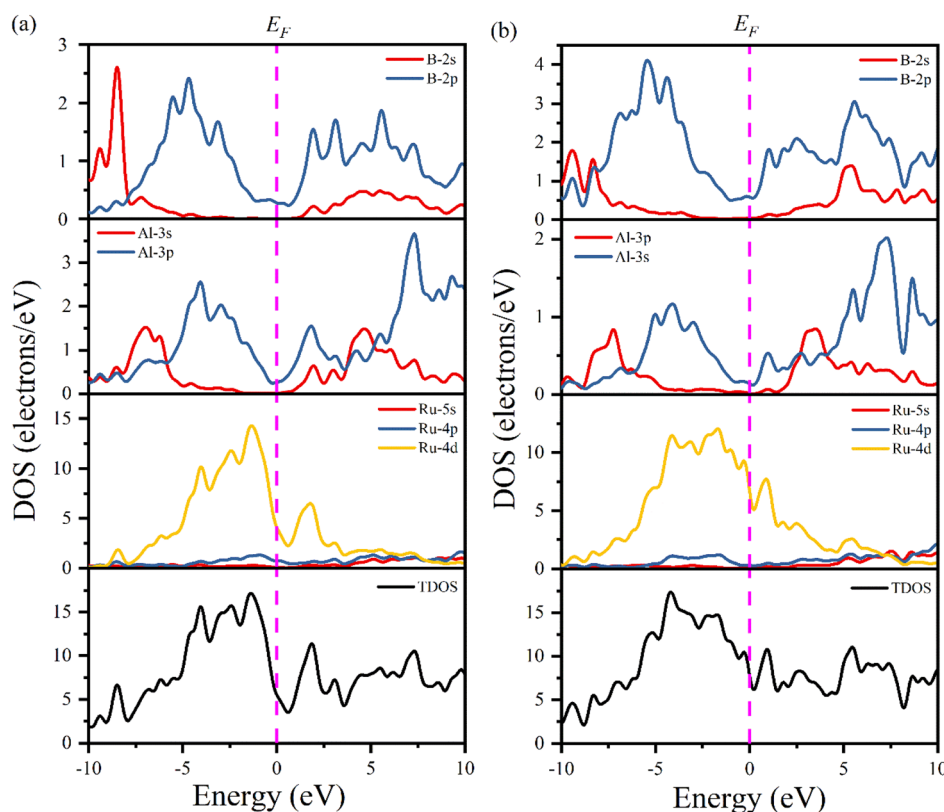


Fig. 6 Total and partial DOS of (a) $\text{Ru}_4\text{Al}_3\text{B}_2$ and (b) $\text{Ru}_9\text{Al}_3\text{B}_8$ at 0 GPa.



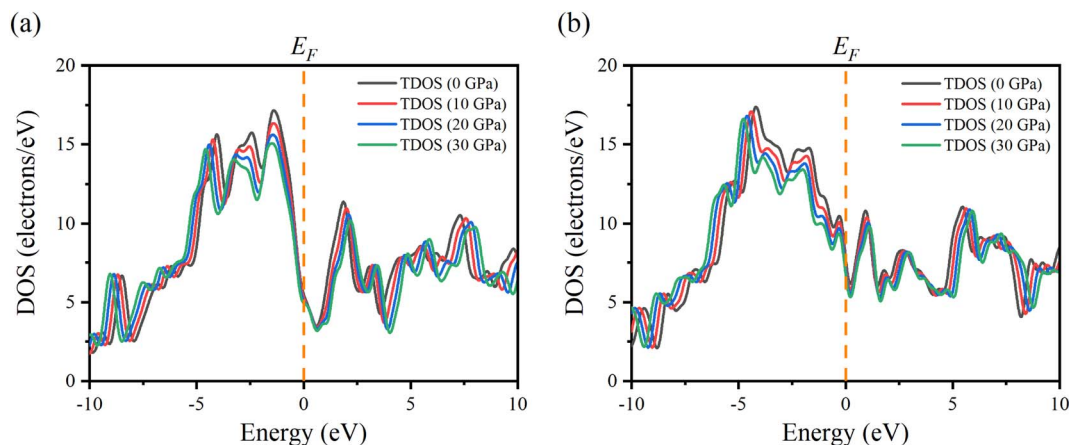


Fig. 7 Changes of TDOS of (a) $\text{Ru}_4\text{Al}_3\text{B}_2$ and (b) $\text{Ru}_9\text{Al}_3\text{B}_8$ at pressure 0, 10, 20, and 30 GPa.

a rectangular sheet and then a curvy sheet along the Γ -Z direction. At the corners of the BZ, the open surfaces are considered as electron pockets. At the top of the BZ, there are some curvy sheets with funnel like features. In the case of $\text{Ru}_9\text{Al}_3\text{B}_8$, there is an arrowhead shaped surface at the Γ point. Along Γ -A direction, there is concave shaped sheet. Then, there are three convex shaped curvy sheets. And finally, there are

three flat rectangular sheets. Therefore, according to the Fermi surface, both compounds contain only electron like sheets.

3.4 Bond population analysis and electronic charge density

The Mulliken population analysis (MPA) is a commonly used technique to study the bonding characteristics of $\text{Ru}_4\text{Al}_3\text{B}_2$ and $\text{Ru}_9\text{Al}_3\text{B}_8$ (Table 2). From Table 2, it can be seen that there is no negative value of population in $\text{Ru}_4\text{Al}_3\text{B}_2$. So, only bonding-type

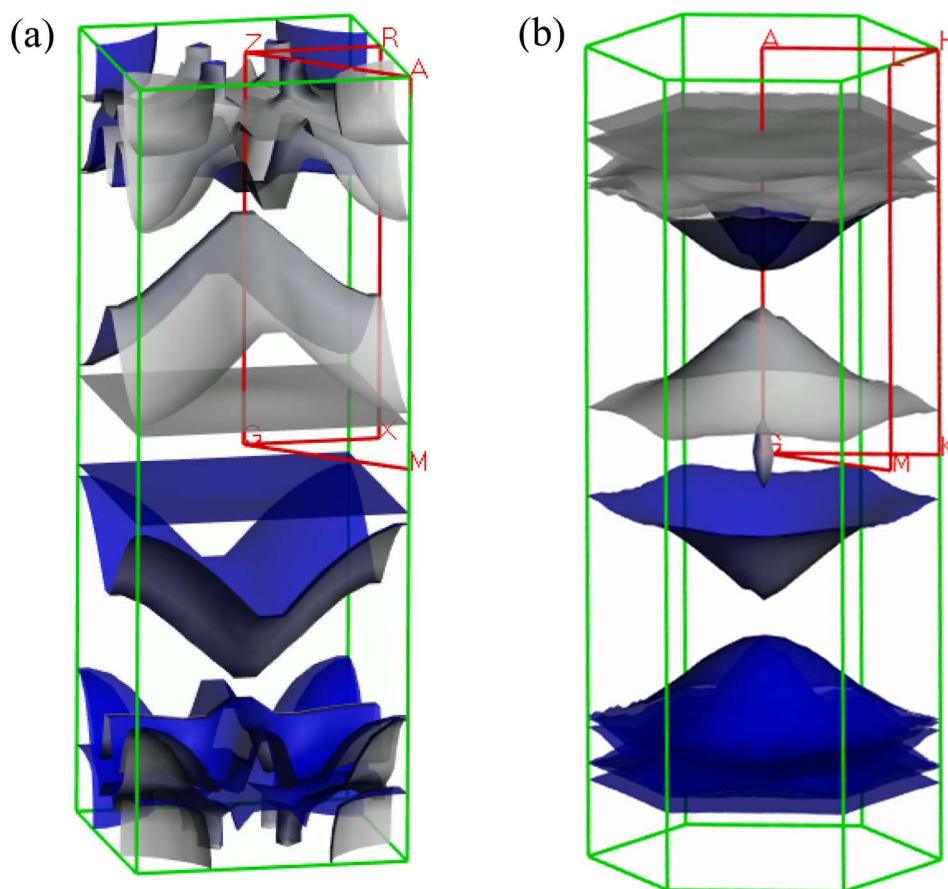


Fig. 8 Fermi surface of metallic (a) $\text{Ru}_4\text{Al}_3\text{B}_2$ and (b) $\text{Ru}_9\text{Al}_3\text{B}_8$ at 0 GPa.



Table 2 Calculated Mulliken bond number n^{μ} , bond overlap population P^{μ} , and bond length d^{μ} (Å), and Mulliken charge (e) of $\text{Ru}_4\text{Al}_3\text{B}_2$ and $\text{Ru}_9\text{Al}_3\text{B}_8$

| Compound | Bond | n^{μ} | P^{μ} | d^{μ} | Species | Mulliken atomic populations | | | | Mulliken charge |
|------------------------------------|-------|-----------|-----------|-----------|---------|-----------------------------|------|------|-------|-----------------|
| | | | | | | s | p | d | Total | |
| $\text{Ru}_4\text{Al}_3\text{B}_2$ | Ru–B | 4 | 0.82 | 2.14837 | Ru | 2.26 | 6.57 | 7.21 | 16.04 | −0.04 |
| | Ru–B | 8 | 0.58 | 2.27323 | Ru | 2.31 | 6.79 | 7.35 | 16.45 | −0.45 |
| | Al–B | 4 | 0.20 | 2.33657 | Al | 0.74 | 1.71 | — | 2.46 | 0.54 |
| | Ru–Al | 8 | 0.37 | 2.55838 | Al | 0.71 | 1.70 | — | 2.41 | 0.59 |
| | Ru–Al | 4 | 0.33 | 2.58894 | Al | 0.66 | 1.69 | — | 2.35 | 0.65 |
| | Ru–Al | 4 | 0.12 | 2.63260 | B | 1.01 | 2.35 | — | 3.36 | −0.36 |
| | Al–B | 8 | 0.04 | 2.64052 | | | | | | |
| | Ru–Al | 8 | 0.18 | 2.86438 | | | | | | |
| $\text{Ru}_9\text{Al}_3\text{B}_8$ | Ru–B | 6 | 0.44 | 2.19800 | Ru | 2.22 | 6.56 | 7.16 | 15.94 | 0.06 |
| | Ru–B | 6 | 0.74 | 2.19897 | Ru | 2.16 | 6.46 | 7.12 | 15.74 | 0.26 |
| | Ru–B | 6 | 0.44 | 2.25404 | Al | 0.72 | 1.60 | — | 2.32 | 0.68 |
| | Ru–B | 6 | −0.12 | 2.27027 | B | 1.02 | 2.31 | — | 3.33 | −0.33 |
| | Ru–B | 6 | −0.13 | 2.35506 | B | 0.94 | 2.45 | — | 3.40 | −0.40 |
| | Al–B | 3 | 0.14 | 2.43169 | B | 0.95 | 2.49 | — | 3.44 | −0.44 |
| | Ru–Al | 3 | 0.33 | 2.45700 | | | | | | |
| | Ru–Al | 6 | 0.27 | 2.65051 | | | | | | |
| | Al–B | 6 | 0.03 | 2.67850 | | | | | | |
| | Ru–Al | 6 | 0.11 | 2.87117 | | | | | | |

interaction is present there. But it is different for $\text{Ru}_9\text{Al}_3\text{B}_8$ as two Ru–B bonds have a negative population. As a result, bond overlap population values for $\text{Ru}_9\text{Al}_3\text{B}_8$ indicate the presence of interactions of both the bonding-type and anti-bonding-type. The Mulliken charge analysis (Table 2) confirmed that electron is transferred from Al to Ru and B atoms in $\text{Ru}_4\text{Al}_3\text{B}_2$, while in $\text{Ru}_9\text{Al}_3\text{B}_8$ structure, the electron is transferred from Ru and Al to B

atoms, respectively. The degree of electron transfer is different from their actual valence such as +3 for Ru, +3 for Al and −3 for B. This result revealed the existence of covalency between constituent atoms in both compounds. From bond population analysis, it is observed that Ru–B, Ru–Al and Al–B bonds possess mixed (both ionic and covalent) bonding nature. Therefore, both ionic and covalent bonds are contributed to form the crystal structures.

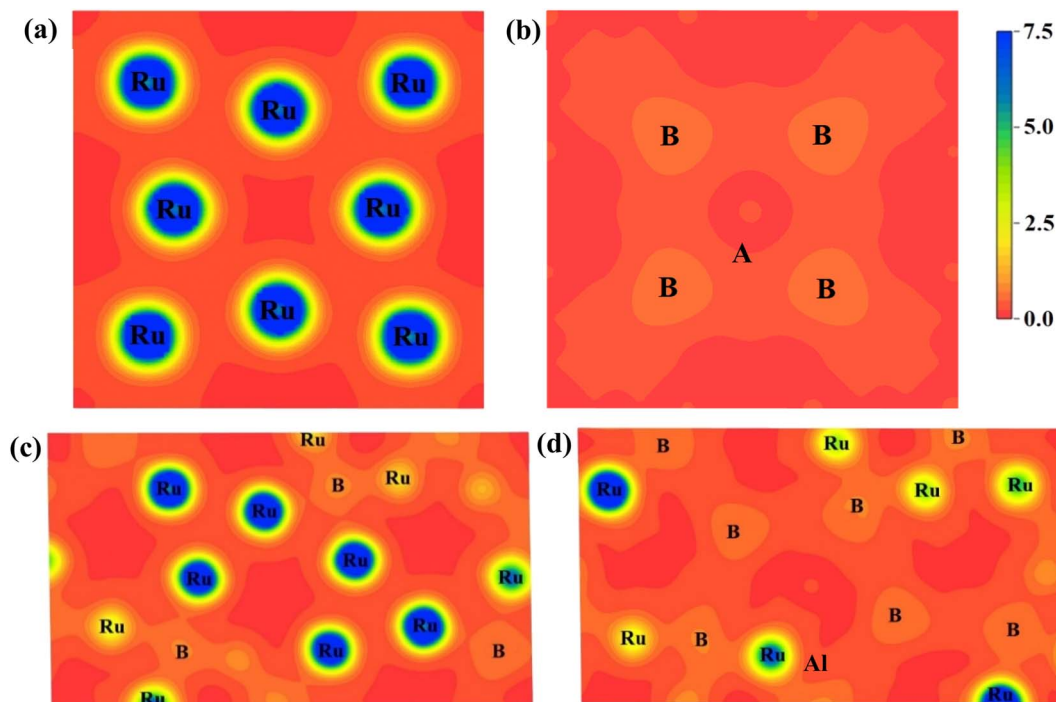
**Fig. 9** Charge density distribution in (111) plane for (a) $\text{Ru}_4\text{Al}_3\text{B}_2$, (b) $\text{Ru}_9\text{Al}_3\text{B}_8$ and in (110) plane for (c) $\text{Ru}_4\text{Al}_3\text{B}_2$, (d) $\text{Ru}_9\text{Al}_3\text{B}_8$. The charge density scale is shown on the upper-right.

Table 3 Elastic constants C_{ij} (GPa) and Cauchy pressure C'' (GPa) of $\text{Ru}_4\text{Al}_3\text{B}_2$ and $\text{Ru}_9\text{Al}_3\text{B}_8$ at different pressures (GPa)

| Compound | P | C_{11} | C_{12} | C_{13} | C_{33} | C_{44} | C_{66} | C'' |
|------------------------------------|-----|----------|----------|----------|----------|----------|----------|--------|
| $\text{Ru}_4\text{Al}_3\text{B}_2$ | 0 | 405.75 | 147.25 | 111.64 | 464.74 | 96.65 | 93.92 | 50.60 |
| | 10 | 473.07 | 179.49 | 143.68 | 535.00 | 116.44 | 110.47 | 63.05 |
| | 20 | 544.13 | 214.41 | 179.99 | 600.28 | 133.57 | 123.94 | 80.84 |
| | 30 | 595.76 | 242.97 | 205.67 | 660.87 | 149.53 | 133.08 | 93.44 |
| $\text{Ru}_9\text{Al}_3\text{B}_8$ | 0 | 425.89 | 217.25 | 155.95 | 500.54 | 138.50 | — | 78.75 |
| | 10 | 488.40 | 254.64 | 186.54 | 556.30 | 157.68 | — | 96.96 |
| | 20 | 539.35 | 289.50 | 232.71 | 638.64 | 172.86 | — | 116.64 |
| | 30 | 600.48 | 325.24 | 260.62 | 691.11 | 191.02 | — | 134.22 |

These results are consistent with the Poisson analysis (previous section) and charge density profile (next section) of the compounds. Bond length of different bonds are also shown in Table 2. Ru–Al has the largest bond length for both compounds. All the bonds have smaller bond length than 3 Å, which is normal for a metal since metallic bonds are shorter in size.³⁹

We projected the electronic charge density distribution around the atoms within the unit cell to show the bonding characteristic and charge transfer among the atoms of $\text{Ru}_4\text{Al}_3\text{B}_2$ and $\text{Ru}_9\text{Al}_3\text{B}_8$. Fig. 9 depicts the charge density ($e/\text{\AA}^3$) distribution for the compounds in (111) and (110) crystallographic planes, and the scale bar (0.0 to 7.5). Both of the under-investigation compounds have shown an asymmetric charge distribution for various atomic species. In the mapping photos, the blue hue indicates the degree of charge accumulation, while the red color denotes charge depletion. The electron density surrounding Ru atoms is extremely high in comparison to B and Al atoms, according to the charge density distribution in the (111) plane of both compounds. In fact, the charge density around Al atoms is absent in this plane. Only B atoms in the compound $\text{Ru}_9\text{Al}_3\text{B}_8$ show a little charge. The charge distribution map in the (110) plane is very much different. For $\text{Ru}_4\text{Al}_3\text{B}_2$, B atoms show very little charge density with the Al atom showing the slightest amount of density at the center. For $\text{Ru}_9\text{Al}_3\text{B}_8$, the charge density around Ru atoms is very high. Very little charge around B atoms is also found with a trace amount of charge around the Al atom found near the center. The charge distribution in different planes of the compounds varies, which means that it is expected for both $\text{Ru}_4\text{Al}_3\text{B}_2$ and $\text{Ru}_9\text{Al}_3\text{B}_8$ to have anisotropy in their charge distribution. From Fig. 9, it can be seen that covalent bond dominates in both compounds.

3.5 Elastic properties

The elastic constants are crucial in determining mechanical stability, or a material's response to macroscopic stress. There are six independent elastic constants for the tetragonal phase and five for the hexagonal phase have been calculated and listed in Table 3. The calculated elastic constants of $\text{Ru}_4\text{Al}_3\text{B}_2$ and $\text{Ru}_9\text{Al}_3\text{B}_8$ for the tetragonal and hexagonal phases satisfy the Born stability criteria⁴⁰ at zero and elevated pressure ($P = 0\text{--}30$ GPa) as $C_{11} > |C_{12}|$; $2C_{13}^2 < C_{33}(C_{11} + C_{12})$; $C_{44} > 0$; $C_{66} > 0$, where $C_{66} = (C_{11} - C_{12})/2$ for the tetragonal phase.

In addition, some notable characteristics can be evaluated using the elastic stiffness constant, C_{ij} . For both compounds,

the value of $C_{33} > C_{11}$ (Table 3) indicates stronger atomic bonding along the c -axis than the a -axis. Furthermore, in comparison to C_{44} , C_{11} and C_{33} levels are much greater which tells the stiffness of the crystal is much higher in the [100] and [001] directions. This means that more energy is required to cause a change in shape or size along these directions compared to the shear deformation. The Cauchy pressure ($C'' = C_{12} - C_{44}$) in Table 3 is related to the concept of stress in materials and it is a measure of ductility/brittleness.⁴¹ A compound is likely to be ductile and has an ionic bond if Cauchy pressure is positive, and *vice versa*.⁴² Since C'' is positive at 0–30 GPa pressures, $\text{Ru}_4\text{Al}_3\text{B}_2$ and $\text{Ru}_9\text{Al}_3\text{B}_8$ both are ductile and have the dominance of ionic bonding.

The moduli of elasticity are numerical constants that describe the mechanical properties of a material when it is subjected to applied stress. The bulk modulus, B and shear modulus, G can be calculated from the elastic constants utilizing the Voigt–Reuss–Hill (VRH) approximations.^{43–46} Furthermore, the associated formulas and theories to calculate elastic moduli B , G , E (Young modulus) and ν (Poisson ratio) can be found in previous literature.^{47–49} The calculated moduli of elasticity of $\text{Ru}_4\text{Al}_3\text{B}_2$ and $\text{Ru}_9\text{Al}_3\text{B}_8$ are tabulated in Table 4. A relatively large value of B and G implies that both compounds are hard materials. In this study, B increased by 56.70% and 48.71% for $\text{Ru}_4\text{Al}_3\text{B}_2$ and $\text{Ru}_9\text{Al}_3\text{B}_8$ respectively, while G increased by 48.79% and 32.58% for $\text{Ru}_4\text{Al}_3\text{B}_2$ and $\text{Ru}_9\text{Al}_3\text{B}_8$ when applied pressure rises from 0 to 30 GPa. It indicates that for both compounds, it will take more volume stress to change their shape than shear stress. The calculated large values of E of the compounds disclose higher stiffness of the compounds. Under external pressure (0–30 GPa), E is increased by 44.66% and 34.60% for $\text{Ru}_4\text{Al}_3\text{B}_2$ and $\text{Ru}_9\text{Al}_3\text{B}_8$, respectively. Between them, $\text{Ru}_9\text{Al}_3\text{B}_8$ possesses the higher stiffness. Since the acoustic mode is responsible for thermal transport due to its large group velocity but the group velocity is also dependent on Young's modulus and the mass density by the following relation:⁵⁰

$$v_s = \sqrt{\frac{E}{\rho}}$$

From this relation, it is confirmed that the compound with higher mass density has lower group velocity and hence lower the lattice thermal conductivity. According to this identity, the thermal conductivity of $\text{Ru}_4\text{Al}_3\text{B}_2$ and $\text{Ru}_9\text{Al}_3\text{B}_8$ should expected



Table 4 Bulk modulus (B in GPa), shear modulus (G in GPa), and Young's modulus, (E in GPa) of $\text{Ru}_4\text{Al}_3\text{B}_2$ and $\text{Ru}_9\text{Al}_3\text{B}_8$ at different pressures (GPa). The subscripts V, R, and H denote Voigt, Reuss, and Hill approximations, respectively

| Compound | P | B_V | B_R | B_H | G_V | G_R | G_H | E_V | E_R | E_H |
|------------------------------------|-----|--------|--------|--------|--------|--------|--------|--------|--------|--------|
| $\text{Ru}_4\text{Al}_3\text{B}_2$ | 0 | 224.15 | 224.03 | 224.09 | 117.83 | 111.43 | 114.63 | 300.77 | 286.74 | 293.79 |
| | 10 | 268.32 | 268.18 | 268.25 | 136.29 | 130.65 | 133.47 | 349.66 | 337.19 | 343.44 |
| | 20 | 315.26 | 315.18 | 315.22 | 152.49 | 147.27 | 149.88 | 393.96 | 382.27 | 388.13 |
| | 30 | 351.22 | 351.09 | 351.16 | 166.30 | 161.06 | 163.68 | 430.89 | 419.09 | 425.00 |
| $\text{Ru}_9\text{Al}_3\text{B}_8$ | 0 | 267.85 | 267.81 | 267.83 | 131.14 | 126.60 | 128.87 | 338.22 | 328.11 | 333.18 |
| | 10 | 309.84 | 309.84 | 309.84 | 146.81 | 142.03 | 144.42 | 380.35 | 369.62 | 375.00 |
| | 20 | 358.57 | 358.23 | 358.40 | 158.29 | 152.95 | 155.62 | 413.96 | 401.69 | 407.83 |
| | 30 | 398.34 | 398.22 | 398.28 | 173.64 | 168.09 | 170.86 | 454.83 | 442.07 | 448.46 |

to be low and the transport properties would be high. This result is consistent with phonon analysis.

When a material is stretched or compressed, Poisson's ratio, ν represents the ratio of lateral strain to axial strain. It can be used to determine the brittle/malleable nature, compressibility, and bonding force characteristics^{51,52} of a compound. Furthermore, Pugh's ratio (B/G) is also used to determine whether a compound is malleable or not. Interestingly, there is a threshold value of both Poisson's (0.26) and Pugh's ratios (1.75) to determine the malleability/brittleness of a compound. A compound having a value of Poisson's ratio and Pugh's ratio higher than that threshold value should be malleable and *vice versa*. In this study, it can be seen that both Poisson's ratio and Pugh's ratio of both $\text{Ru}_4\text{Al}_3\text{B}_2$ and $\text{Ru}_9\text{Al}_3\text{B}_8$ are above their threshold value. So, both compounds are malleable, *i.e.*, ductile. $\text{Ru}_9\text{Al}_3\text{B}_8$ is more malleable compared to $\text{Ru}_4\text{Al}_3\text{B}_2$ and their malleability increases with pressure. Besides this, Poisson's ratio can also reflect the nature of the bonding of a compound. If $\nu < 0.25$, then covalent bond dominates the compound whereas $\nu \geq 0.25$ indicates ionic characteristics.⁵³ Moreover, if ν is found to be in the range of $0.25 \leq \nu \leq 0.50$, then central force dominates in the solid and non-central force dominates if ν is outside of this range.⁵⁴ From our findings, ionic contribution and central force interaction play a key role in both compounds.

The machinability index, μ_M determines the cutting force, tool wear, and many other aspects of a material. The machinability index, μ_M of a material can be stated as:⁵⁵

$$\mu_M = \frac{B}{C_{44}}$$

From our findings, though the machinability of $\text{Ru}_4\text{Al}_3\text{B}_2$ is more than that of $\text{Ru}_9\text{Al}_3\text{B}_8$, both compounds are suitable to build machines.

The hardness of the materials was calculated using an empirical approach:^{56,57}

$$H_{\text{macro}} = 2 \left[\left(\frac{G}{B} \right)^2 G \right]^{0.585} - 3$$

and

$$H_{\text{micro}} = \frac{(1 - 2\nu)E}{6(1 + \nu)}$$

Both compounds are found to be quite hard and micro hardness is greater than the macro hardness (Table 5) due to the difference in parameters used to calculate them. As expected, the hardness increases with increasing pressure. One interesting thing is that $\text{Ru}_4\text{Al}_3\text{B}_2$ has more macro hardness than that of $\text{Ru}_9\text{Al}_3\text{B}_8$, but it is the opposite in the case of micro hardness.

The ability of a material to resist the propagation of cracks and fractures when subjected to external forces is referred to as fracture toughness, K_{IC} can be determined by using the formula proposed by Niu *et al.*:⁵⁸

$$K_{IC} = V_0^{1/6} G(B/G)^{0.5}$$

where V_0 is the final volume per atom of the unit cell.

The obtained values of K_{IC} for the compounds are listed in Table 5. $\text{Ru}_4\text{Al}_3\text{B}_2$ is more prone to cracks than $\text{Ru}_9\text{Al}_3\text{B}_8$ and the trend suggests that K_{IC} increases with pressure.

The anisotropy factors A_1 , A_2 and A_3 also known as shear anisotropy factors, associated with the $\{100\}$, $\{010\}$ and $\{001\}$ shear planes between $\langle 011 \rangle$ and $\langle 010 \rangle$, $\langle 101 \rangle$ and $\langle 001 \rangle$, and $\langle 110 \rangle$ and $\langle 100 \rangle$ directions, respectively. The variation of the values of A_i ($i = 1, 2, 3$) different from unity implies the anisotropic nature of the compounds under consideration:^{59–61}

$$A_1 = \frac{4C_{44}}{C_{11} + C_{33} - 2C_{13}}$$

Table 5 Poisson's ratio (ν), Pugh's ratio (B/G), Kleinman parameter (ξ), machinability index (μ_M), hardness values, (H_{macro} and H_{micro} in GPa), and fracture toughness, (K_{IC} in MPa $\text{m}^{0.5}$) of $\text{Ru}_4\text{Al}_3\text{B}_2$ and $\text{Ru}_9\text{Al}_3\text{B}_8$ at different pressures (GPa)

| Compound | P | ν | B/G | μ_M | H_{macro} | H_{micro} | K_{IC} |
|------------------------------------|-----|-------|-------|---------|--------------------|--------------------|----------|
| $\text{Ru}_4\text{Al}_3\text{B}_2$ | 0 | 0.281 | 1.95 | 2.318 | 11.63 | 16.70 | 2.42 |
| | 10 | 0.287 | 2.01 | 2.304 | 12.48 | 18.99 | 2.84 |
| | 20 | 0.295 | 2.10 | 2.360 | 12.71 | 20.51 | 3.24 |
| | 30 | 0.298 | 2.15 | 2.348 | 13.16 | 22.01 | 3.56 |
| $\text{Ru}_9\text{Al}_3\text{B}_8$ | 0 | 0.293 | 2.08 | 1.934 | 11.58 | 17.81 | 2.76 |
| | 10 | 0.298 | 2.15 | 1.965 | 12.02 | 19.42 | 3.12 |
| | 20 | 0.310 | 2.30 | 2.073 | 11.44 | 19.68 | 3.47 |
| | 30 | 0.312 | 2.33 | 2.085 | 12.04 | 21.38 | 3.81 |



$$A_2 = \frac{4C_{55}}{C_{22} + C_{33} - 2C_{23}}$$

$$A_3 = \frac{4C_{66}}{C_{11} + C_{22} - 2C_{12}}$$

Shear anisotropic factors for $\text{Ru}_4\text{Al}_3\text{B}_2$ and $\text{Ru}_9\text{Al}_3\text{B}_8$ are calculated and provided in Table 6 and the results reveal that $\text{Ru}_4\text{Al}_3\text{B}_2$ is more anisotropic whereas $\text{Ru}_9\text{Al}_3\text{B}_8$ has less anisotropy.

3.6 Thermophysical properties

Different thermo-physical properties of a compound are firmly accompanied by the sound velocity through the material as well as Debye temperature. The construction of musical instruments, transducer design, acoustic application underwater and noise attenuation in a jet engine, *etc.* depend greatly on a material's acoustic characteristics. Thermal conductivity is another crucial physical characteristic for spintronic and electronic device applications at high temperatures.

3.6.1 Acoustic velocities. Acoustic velocity is the rate at which sound waves travel through a solid medium. The elastic properties of the material dictate it, and it may be characterized using two forms of velocity: longitudinal velocity (*P*-wave velocity) and transverse velocity (*S*-wave velocity). In a crystalline material, the transverse and longitudinal sound velocities are determined from:⁶²

$$v_t = \sqrt{\frac{G}{\rho}} \text{ and } v_l = \sqrt{\frac{3B + 4G}{3\rho}}$$

where ρ is the density of the material.

The mean sound velocity, v_m can be obtained in terms of the transverse, v_t and longitudinal, v_l sound velocities:⁶²

$$v_m = \left[\frac{1}{3} \left(\frac{2}{v_t^3} + \frac{1}{v_l^3} \right) \right]^{-\frac{1}{3}}$$

The calculated pressure dependent longitudinal velocity of the compounds is ~ 1.5 to ~ 2 times higher than that of the transverse velocity, as can be seen in Table 7. From our study, it is found that $\text{Ru}_9\text{Al}_3\text{B}_8$ is harder than $\text{Ru}_4\text{Al}_3\text{B}_2$ as the sound

Table 6 Shear anisotropic factors (A_1 , A_2 , and A_3) of $\text{Ru}_4\text{Al}_3\text{B}_2$ and $\text{Ru}_9\text{Al}_3\text{B}_8$ at P (0–30) GPa

| Compound | Pressure (GPa) | A_1 | A_2 | A_3 |
|------------------------------------|----------------|-------|-------|-------|
| $\text{Ru}_4\text{Al}_3\text{B}_2$ | 0 | 0.597 | 0.597 | 0.727 |
| | 10 | 0.646 | 0.646 | 0.753 |
| | 20 | 0.681 | 0.681 | 0.752 |
| | 30 | 0.708 | 0.708 | 0.754 |
| $\text{Ru}_9\text{Al}_3\text{B}_8$ | 0 | 0.902 | 0.902 | 1.000 |
| | 10 | 0.939 | 0.939 | 1.000 |
| | 20 | 0.970 | 0.970 | 1.000 |
| | 30 | 0.992 | 0.992 | 1.000 |

Table 7 Transverse sound velocity v_t (ms^{-1}), longitudinal sound velocity v_l (ms^{-1}), average sound wave velocity v_m (ms^{-1}), acoustic impedance Z ($\text{Rayl} = \text{kg m}^{-2} \text{s}^{-1}$) and radiation factor $\sqrt{G/\rho^3}$ ($\text{m}^4 \text{kg}^{-1} \text{s}^{-1}$), and density ρ (g cm^{-3}) of $\text{Ru}_4\text{Al}_3\text{B}_2$ and $\text{Ru}_9\text{Al}_3\text{B}_8$ at different pressure (GPa)

| Compound | P | v_l | v_t | v_m | Z | $\sqrt{G/\rho^3}$ | ρ |
|------------------------------------|-----|---------|---------|---------|--------|-------------------|--------|
| $\text{Ru}_4\text{Al}_3\text{B}_2$ | 0 | 6922.90 | 3817.72 | 4254.46 | 30.025 | 0.485 | 7.865 |
| | 10 | 7380.61 | 4036.57 | 4501.20 | 33.065 | 0.493 | 8.191 |
| | 20 | 7794.16 | 4204.50 | 4693.24 | 35.648 | 0.496 | 8.479 |
| | 30 | 8073.07 | 4328.40 | 4833.68 | 37.815 | 0.495 | 8.737 |
| $\text{Ru}_9\text{Al}_3\text{B}_8$ | 0 | 7233.31 | 3916.16 | 4370.22 | 32.908 | 0.466 | 8.403 |
| | 10 | 7599.14 | 4074.31 | 4549.93 | 35.447 | 0.468 | 8.700 |
| | 20 | 7943.85 | 4165.77 | 4659.22 | 37.357 | 0.465 | 8.968 |
| | 30 | 8244.11 | 4306.74 | 4818.12 | 39.674 | 0.468 | 9.212 |

velocities are higher in it. As expected, the velocities become higher when pressure is applied, and the average sound velocity increases by 13.61% and 10.25% for $\text{Ru}_4\text{Al}_3\text{B}_2$ and $\text{Ru}_9\text{Al}_3\text{B}_8$, respectively when the pressure is increased to 30 GPa. It indicates that the effect of pressure on $\text{Ru}_4\text{Al}_3\text{B}_2$ is more than that of $\text{Ru}_9\text{Al}_3\text{B}_8$.

The acoustic impedance, Z , of a material is found in:⁶³

$$Z = \sqrt{\rho G}$$

According to the above equation, a material with higher density and shear modulus has a higher acoustic impedance. In our present study, acoustic impedance $\text{Ru}_9\text{Al}_3\text{B}_8$ is higher than $\text{Ru}_4\text{Al}_3\text{B}_2$ and it increases with increasing pressure.

The intensity of sound radiation is an important parameter in the design of acoustic insulation and soundproofing materials, which aim to reduce the amount of sound energy that is transmitted from one space to another. For a particular driving source, the radiation intensity, I depends on the surface velocity. This is related to the modulus of rigidity and density as:⁶³

$$I \approx \sqrt{G/\rho^3}$$

where $\sqrt{G/\rho^3}$ is called the radiation factor.

The values of Z and I are tabulated in Table 7. Both compounds have a similar intensity of sound radiation.

3.6.2 Debye and melting temperature. The Debye temperature, Θ_D is estimated using the elastic constants at low temperatures because vibrational excitations are solely caused by acoustic vibrations at low temperatures, and the following equations:^{62,64}

$$\Theta_D = \frac{h}{k_B} \left[\left(\frac{3n}{4\pi} \right) \frac{N_A}{M} \right]^{1/3} v_m$$

where h stands for Planck constant, k_B is Boltzmann's constant, N_A is Avogadro's number, ρ indicates mass density, M is the molecular weight, and n is the number of atoms within the unit cell. The estimated large value of the Debye temperature (Table 8) for both $\text{Ru}_4\text{Al}_3\text{B}_2$ and $\text{Ru}_9\text{Al}_3\text{B}_8$ suggests that high melting point, high thermal conductivity, and high stiffness are expected. Since Θ_D has an inverse relation with specific heat



Table 8 The Debye temperature Θ_D (K), melting temperature T_m (K), thermal expansion coefficient α (K^{-1}), the wavelength of the dominant phonon at 300 K λ_{dom} (m), heat capacity per unit volume ρC_P ($J m^{-3} K^{-1}$), Grüneisen parameter γ , minimum thermal conductivity k_{min} ($W m^{-1} K^{-1}$), and lattice thermal conductivity k_{ph}^* ($W m^{-1} K^{-1}$) of $Ru_4Al_3B_2$ and $Ru_9Al_3B_8$ at various pressures (GPa)

| Compound | <i>P</i> | Θ_D | T_m | α ($\times 10^{-5}$) | ρC_P ($\times 10^6$) | λ_{dom} ($\times 10^{-12}$) | γ | k_{min} | k_{ph}^* |
|---------------|----------|------------|---------|-------------------------------|------------------------------|---------------------------------------|----------|-----------|------------|
| $Ru_4Al_3B_2$ | 0 | 555.20 | 2268.37 | 1.396 | 3.48 | 178.20 | 1.664 | 1.128 | 24.224 |
| | 10 | 595.42 | 2575.72 | 1.199 | 3.63 | 188.54 | 1.693 | 1.226 | 28.379 |
| | 20 | 628.00 | 2886.82 | 1.068 | 3.75 | 196.58 | 1.741 | 1.308 | 30.958 |
| | 30 | 653.29 | 3132.59 | 0.976 | 3.87 | 202.47 | 1.762 | 1.374 | 33.598 |
| $Ru_9Al_3B_8$ | 0 | 591.80 | 2382.47 | 1.242 | 3.89 | 183.05 | 1.728 | 1.247 | 18.403 |
| | 10 | 623.31 | 2653.66 | 1.108 | 4.03 | 190.58 | 1.762 | 1.329 | 20.370 |
| | 20 | 644.76 | 2929.99 | 1.028 | 4.15 | 195.16 | 1.839 | 1.389 | 20.338 |
| | 30 | 672.75 | 3192.10 | 0.936 | 4.26 | 201.82 | 1.852 | 1.462 | 22.545 |

capacity, these compounds will have fairly low values of specific heat capacity.

Understanding the melting behavior of solids is important in materials science and engineering, as it affects the processing and performance of materials in various applications. The following equation⁶⁵ can be used to determine the melting temperature T_m of solids using the elastic constants:

$$T_m = 354 \text{ K} + (4.5 \text{ K GPa}^{-1}) \left(\frac{2C_{11} + C_{33}}{3} \right) \pm 300 \text{ K}$$

The values of T_m for $Ru_4Al_3B_2$ and $Ru_9Al_3B_8$ are listed in Table 8. As we can see, both compounds have very high melting temperatures, and hence their possible applicability lies in thermally harsh conditions. The effect of pressure on the melting temperature is enormous as the value of T_m rises sharply with temperature with 38% for $Ru_4Al_3B_2$ and 34% for $Ru_9Al_3B_8$ when the pressure increases from 0 to 30 GPa.

The dominant phonon wavelength, λ_{dom} can have important effects on the thermal and mechanical properties of the solid, such as its thermal conductivity, specific heat capacity, and phonon scattering. The dominant phonon wavelength for $Ru_4Al_3B_2$ and $Ru_9Al_3B_8$ at 300 K has been calculated by using the following relationship:⁶⁶

$$\lambda_{dom} = \frac{112.566 v_m}{T} \times 10^{-12}$$

where v_m denotes the average sound velocity in ms^{-1} and T denotes the temperature in K. The obtained value of λ_{dom} for $Ru_4Al_3B_2$ and $Ru_9Al_3B_8$ suggested that $Ru_9Al_3B_8$ have higher phonon wavelength compared to $Ru_4Al_3B_2$.

3.6.3 The Grüneisen parameter. The Grüneisen parameter, γ , of $Ru_4Al_3B_2$ and $Ru_9Al_3B_8$ has been calculated using the following relation:⁶⁷

$$\gamma = \frac{3}{2} \left(\frac{1 + \nu}{2 - 3\nu} \right)$$

where ν is the Poisson's ratio which can also be calculated from longitudinal (v_l) and transverse (v_t) sound waves using the relation:^{67,68}

$$\nu = \frac{1 - 2(v_t/v_l)^2}{2 - 2(v_t/v_l)^2}$$

The calculated values γ of the compounds with varying pressure are tabulated in Table 8 and γ rises with pressure. The value of γ is high for both compounds indicating strong anharmonicity, hence thermal conductivity will be low for both compounds. Additionally, a large value of γ implies that the compound's thermal properties, such as thermal expansion, specific heat, and thermal conductivity, are highly sensitive to changes in temperature and pressure. Therefore, both $Ru_4Al_3B_2$, and $Ru_9Al_3B_8$ can be useful for applications in thermoelectric devices, temperature sensors, and other areas where precise control of thermal properties is necessary.

3.6.4 Minimum and lattice thermal conductivity. Minimum thermal conductivity, k_{min} refers to the lowest possible thermal conductivity that a material or substance can possess. Clarke's formula can be used to calculate the minimum thermal conductivity k_{min} at high temperatures as:⁶⁶

$$k_{min} = k_B v_m \left(\frac{n N_A \rho}{M} \right)^{2/3}$$

the Boltzmann constant, k_B , Avogadro's number N_A , the mass density ρ , the number of atoms in a molecule n , the average sound velocity v_m , and the molecular weight M , are all included in this expression. The values of k_{min} of both compounds are listed in Table 8 and they have fairly low values. It is worth noting that materials with extremely low thermal conductivity can have useful applications in insulation or thermoelectric devices. For thermal barrier coating (TBC) applications, k_{min} should be equal to or smaller than the limiting value of $1.25 \text{ W m}^{-1} K^{-1}$,⁶⁹ and according to our study, both $Ru_4Al_3B_2$ and $Ru_9Al_3B_8$ can be used as TBC material at ambient pressure.

Lattice thermal conductivity, k_{ph} , on the other hand, refers to the contribution of phonons to the overall thermal conductivity of a material. Using Slack's model, the lattice thermal conductivity can be calculated by using the empirical formula:⁷⁰

$$k_{ph} = A \frac{M_{av} \Theta_D^3 \delta}{\gamma^2 n^{2/3} T}$$

where M_{av} is the average atomic mass of a crystal, Θ_D is the Debye temperature, δ is the cubic root of the average atomic volume, γ is the Grüneisen parameter, n is the number of atoms in the unit cell, and T is the temperature.

The factor $A(\gamma)$ is determined by Julian's formula,⁷¹



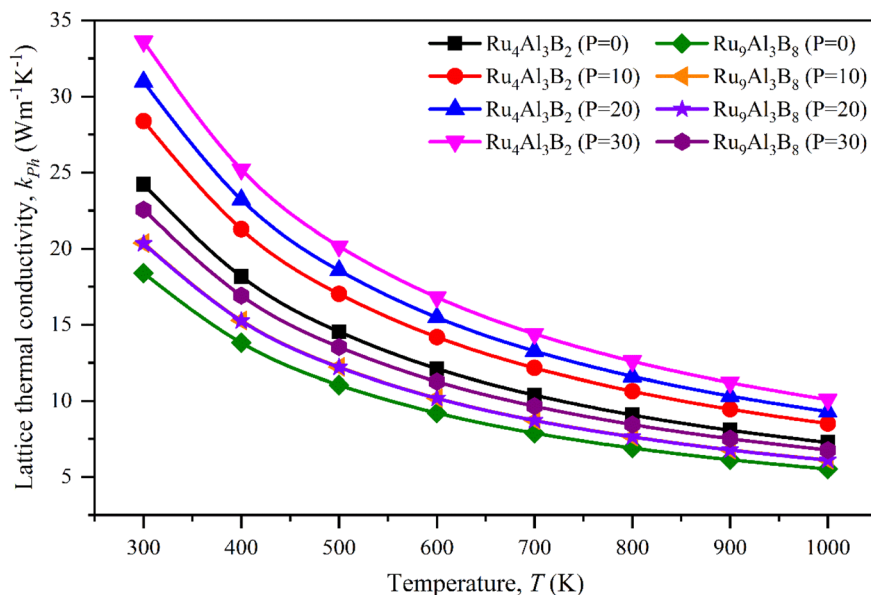


Fig. 10 Lattice thermal conductivity of $\text{Ru}_4\text{Al}_3\text{B}_2$ and $\text{Ru}_9\text{Al}_3\text{B}_8$ for pressure 0–30 GPa as a function of temperature.

$$A(\gamma) = \frac{5.72 \times 10^7 \times 0.849}{2 \times \left(1 - \frac{0.514}{\gamma} + \frac{0.228}{\gamma^2} \right)}$$

The lattice thermal conductivity calculated for $\text{Ru}_4\text{Al}_3\text{B}_2$ and $\text{Ru}_9\text{Al}_3\text{B}_8$ at room temperature (300 K) is listed in Table 8 and the temperature dependence on k_{ph} is shown in Fig. 10. With increasing pressure, k_{ph} rises for $\text{Ru}_4\text{Al}_3\text{B}_2$. However, there is an exception in the case of $\text{Ru}_9\text{Al}_3\text{B}_8$. When 20 GPa of pressure is applied, k_{ph} decreases instead of increasing. It increases again when 30 GPa of pressure is applied. From Fig. 10, it can be said that $\text{Ru}_4\text{Al}_3\text{B}_2$ has higher lattice thermal conductivity than $\text{Ru}_9\text{Al}_3\text{B}_8$ for all pressure ranges. The exponential decrease of the lattice thermal conductivity with the increase in temperature is perceived for both compounds.

3.7 Optical properties

Dielectric function $\epsilon(\omega)$, refractive index $n(\omega)$, absorption coefficient $\alpha(\omega)$, optical conductivity $\sigma(\omega)$, reflectivity $R(\omega)$, and energy loss function $L(\omega)$ of $\text{Ru}_4\text{Al}_3\text{B}_2$ and $\text{Ru}_9\text{Al}_3\text{B}_8$ were calculated since they are useful to determine the optical properties of a compound. The pressure induced optical parameters of the compounds are depicted in Fig. 11 and 12 for incident energies up to 32.5 eV along the [100] direction. The dielectric function, $\epsilon(\omega) = \epsilon_1(\omega) + i\epsilon_2(\omega)$ is a complex-valued quantity that describes the response of a material to an external electric field, where $\epsilon_1(\omega)$ and $\epsilon_2(\omega)$ are real and imaginary parts of $\epsilon(\omega)$. The real part, $\epsilon_1(\omega)$ in Fig. 11(a) has a prominent peak in the range 0–0.5 eV and falls below zero at ~ 0.5 eV for both compounds and remains below that mark until ~ 28.3 eV and ~ 30.1 eV is reached for $\text{Ru}_4\text{Al}_3\text{B}_2$ and $\text{Ru}_9\text{Al}_3\text{B}_8$, respectively, and shows metallic characteristic with a strong Drude peak at low energy. The greatest value of $\epsilon_2(\omega)$ occurs at zero energy and falls with

increasing photon energy, as seen in Fig. 11(b) and 12(b). This is a very common incidence in metallic systems. It can be seen from the figures that the value of $\epsilon_2(\omega)$ become zero at ~ 24.8 eV and ~ 28.2 eV for $\text{Ru}_4\text{Al}_3\text{B}_2$ and $\text{Ru}_9\text{Al}_3\text{B}_8$, respectively, predicting that the compounds will show transparency above that energy value. Fig. 11(c) and 12(c) depict the absorption of the compounds $\text{Ru}_4\text{Al}_3\text{B}_2$ and $\text{Ru}_9\text{Al}_3\text{B}_8$, respectively. In both cases, the absorption starts at 0 eV, which is another indication of their metallic characteristic. For $\text{Ru}_4\text{Al}_3\text{B}_2$, the peak absorption is at ~ 10.7 eV and the peak value shifts towards slightly higher energy with pressure. Absorption decreases to some extent with energy till ~ 21 eV and after that, it falls drastically. For $\text{Ru}_9\text{Al}_3\text{B}_8$, absorption reaches its peak at ~ 11 eV and remains nearly the same up to ~ 23.7 eV. It falls rapidly after that value. It is noteworthy that the absorption coefficient is of the order of $\sim 10^5 \text{ cm}^{-1}$ which concluded that both compounds should be excellent solar absorbers and would be suitable for absorber in photovoltaic device applications. The reflectivity spectra start at 95%, and 96% for $\text{Ru}_4\text{Al}_3\text{B}_2$ and $\text{Ru}_9\text{Al}_3\text{B}_8$, respectively, are shown in Fig. 11(d) and 12(d).

The maximum value of the reflectivity is found in the IR and visible range of photon energy. Furthermore, the reflectance spectra for $\text{Ru}_4\text{Al}_3\text{B}_2$ and $\text{Ru}_9\text{Al}_3\text{B}_8$ in the 0 to 30 eV photon energy range never drop below 38% and 42%, respectively. The value of reflectivity spectra of these two compounds is higher than that of other metallic borides of Cr_4AlB_4 (ref. 72) and Zr_3CdB_4 .⁷³ Based on our calculations, $\text{Ru}_9\text{Al}_3\text{B}_8$ can be used as coatings on space crafts as it can avoid solar heating. In Fig. 11(e, f) and 12(e, f), respectively, the real, $n(\omega)$, and imaginary, $k(\omega)$, components of the refractive indices of $\text{Ru}_4\text{Al}_3\text{B}_2$ and $\text{Ru}_9\text{Al}_3\text{B}_8$ are depicted. At zero photon energy/frequency, the values of n are 51.28 and 52.92, respectively.

A high refractive index is a necessary condition for photonics and optoelectronic applications, such as LEDs, OLEDs, mini-



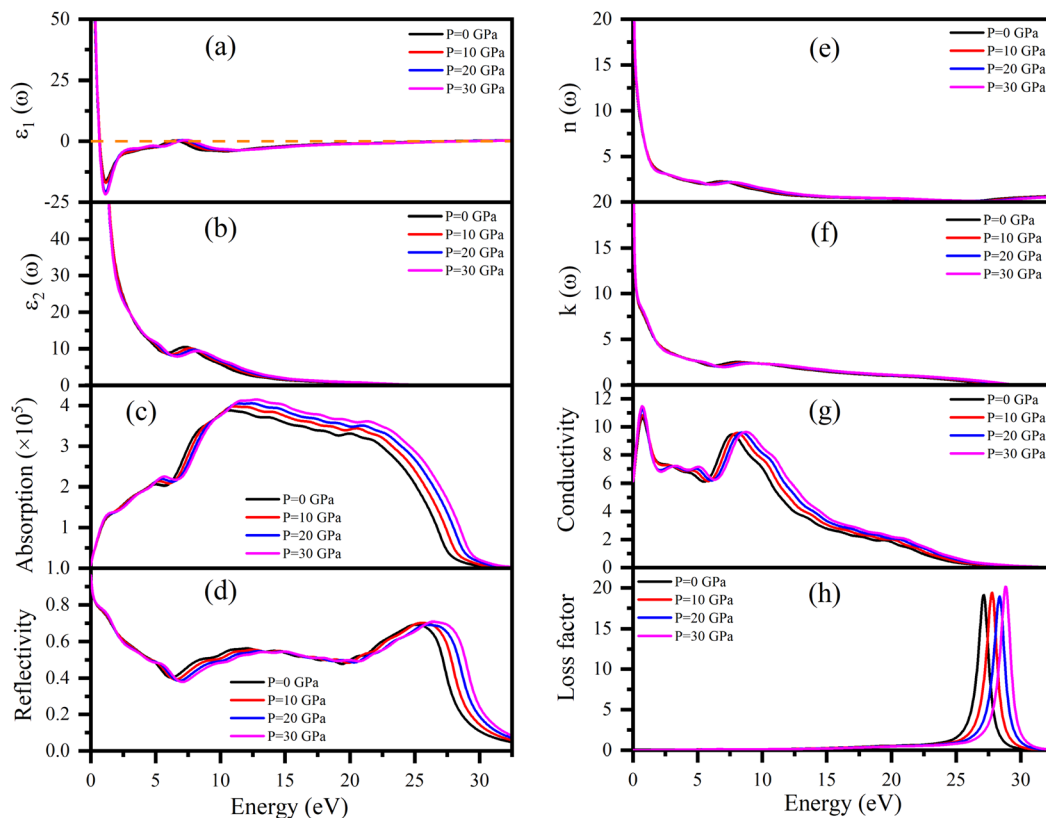


Fig. 11 (a) $\epsilon_1(\omega)$, (b) $\epsilon_2(\omega)$, (c) absorption coefficient, (d) reflectivity, (e) $n(\omega)$, (f) $k(\omega)$, (g) optical conductivity, and (h) energy loss function of $\text{Ru}_4\text{Al}_3\text{B}_2$ in the [100] direction under pressure from 0–30 GPa as a function of photon energy.

LEDs, micro-LEDs, and QDLEDs screens. These two compounds have very high values of $n(0)$ and can be used in micro LED screens that will be used in virtual reality/augmented reality headsets which need very high pixel per inch (PPI) screens. The spectrum of $k(\omega)$ shows that the studied compounds will have low-energy light (IR) absorption since its peak is in the 0–1 eV range. The effect of pressure on both n and k is negligible. Optical conductivity starts at 0 eV of photon energy (Fig. 11(f) and 12(f)), which further confirms the metallic character. For both $\text{Ru}_4\text{Al}_3\text{B}_2$ and $\text{Ru}_9\text{Al}_3\text{B}_8$, photoconductivity rises in the IR region at first and sharply decreases until the visible range is reached. Photoconductivity reaches its next peak at 7.7–8.7 eV for $\text{Ru}_4\text{Al}_3\text{B}_2$ depending on the pressure and at 8.2–9.3 eV for $\text{Ru}_9\text{Al}_3\text{B}_8$. After that, it gradually decreases to zero. One interesting fact is the effect of pressure is evident on $\text{Ru}_9\text{Al}_3\text{B}_8$ in the IR region. Photoconductivity decreases with increasing pressure in this region. The conductivity of a material depends on the number of free charge carriers available to conduct electricity. In the IR region, the energy of the radiation is lower than the energy required to excite electrons from the valence band to the conduction band. Therefore, there are fewer free electrons available for conduction, which leads to a decrease in conductivity.

Optical loss is a property of materials that describes the amount of electromagnetic energy, such as light or infrared radiation, that is lost as it passes through the material. Because

of the relatively high value of $\epsilon_2(\omega)$, it is evident from Fig. 11(h) and 12(h) that neither compound experiences any energy loss up to about 15 eV. Maximum energy loss is observed due to plasma resonance. The peak of the loss function is found to be at 27.0–28.8 eV for $\text{Ru}_4\text{Al}_3\text{B}_2$ and at 29.0–30.5 eV for $\text{Ru}_9\text{Al}_3\text{B}_8$. The reflection and absorption spectra drop dramatically at these energies, and the compounds under study are expected to have high transmittance. The effect of pressure is non-selective for $\text{Ru}_4\text{Al}_3\text{B}_2$, but for $\text{Ru}_9\text{Al}_3\text{B}_8$, there is a clear pattern. The peak value of the loss function of $\text{Ru}_9\text{Al}_3\text{B}_8$ shifts towards higher photon energy while the height of the peak decreases with pressure. In the case of $\text{Ru}_4\text{Al}_3\text{B}_2$, only the position of the peak shifts.

3.8 Thermodynamic properties

Different temperatures and pressures are frequently applied to materials. Therefore, the study of pressure and temperature dependent bulk modulus and thermodynamic properties has an enormous effect on how they are used at high-temperature and pressure in industrial applications. Gibbs2 (ref. 30) program was used to investigate the temperature and pressure dependent thermodynamic properties of $\text{Ru}_4\text{Al}_3\text{B}_2$ and $\text{Ru}_9\text{Al}_3\text{B}_8$, shown in Fig. 13 (a–r). The pressure range was set to 0–100 GPa, and the temperature range was set to 0–1000 K. It was found that no phase transition occurred for both compounds while the specified pressure and temperature were



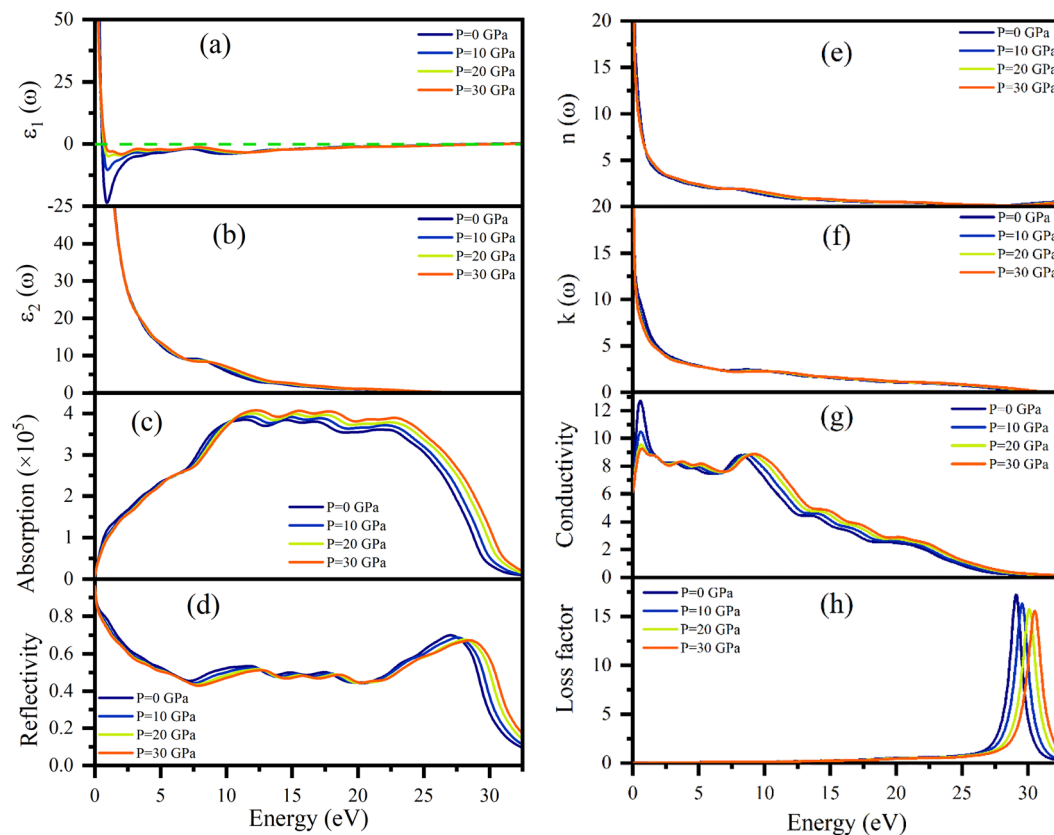


Fig. 12 (a) $\epsilon_1(\omega)$, (b) $\epsilon_2(\omega)$, (c) absorption coefficient, (d) reflectivity, (e) $n(\omega)$, (f) $k(\omega)$, (g) optical conductivity, and (h) energy loss function of $\text{Ru}_9\text{Al}_3\text{B}_8$ in the [100] direction under pressure from 0–30 GPa as a function of the photon energy.

applied. Fig. 13(a and b) shows the temperature and pressure dependence of adiabatic bulk modulus, B of the two compounds at $P = 0$ GPa and $T = 300$ K, respectively. From Fig. 13(a), it is observed that the difference of B between the two compounds is almost double, but both follow the same pattern. Bulk modulus decreases slowly at a low (~ 100 K) temperature range, which is associated with the 3rd law of thermodynamics and after that point, the decrement is much more. The decrease of B with pressure indicates that the compounds become harder at high pressure. At a given T , the bulk modulus, B increases with increasing P , which is a usual characteristic because external stress makes the compound mechanically stronger. Between the two compounds, $\text{Ru}_9\text{Al}_3\text{B}_8$ is stronger due to the higher value of bulk modulus. From Fig. 13(b), it is evident that the bulk modulus, B increases linearly with increasing pressure, P at room temperature (300 K) for both compounds. Fig. 13(c and d) presents the Debye temperature, Θ_D as a function of temperature and pressure and the value of Θ_D decreases with increasing temperature. These curves are similar to that of the bulk modulus. B and Θ_D decrease with temperature since material stiffness also decreases with temperature.⁷⁴ On the other hand, pressure increases the stiffness of the compound and as a result, B and Θ_D also increase. Θ_D increases in a non-linear fashion, between linear and exponential. Specific heat capacity at constant volume, C_V , and at constant pressure, C_P of $\text{Ru}_4\text{Al}_3\text{B}_2$ and $\text{Ru}_9\text{Al}_3\text{B}_8$, as a function of temperature and

pressure, are also shown in Fig. 13(e–h). Heat capacities rise due to phonon thermal softening as temperature increases. The discrepancy between C_P and C_V is related to thermal expansion by anharmonicity effects. C_V follows the Debye equation, which states that in the low temperature region ($T \sim 300$ K), C_V is proportional to T^3 , and at high temperatures ($T > 300$ K), the anharmonic influence on heat capacity is muted and C_V approaches the traditional asymptotic Dulong–Petit limit $C_V = 3nN_Ak_B$ (224.49 J mol^{−1} K^{−1} for $\text{Ru}_4\text{Al}_3\text{B}_2$ and 498.87 J mol^{−1} K^{−1} for $\text{Ru}_9\text{Al}_3\text{B}_8$). At low T , C_P behaves likewise to C_V while C_P is slightly greater than C_V at higher temperatures. From Fig. 13(g and h), it is observed that both C_V and C_P decreases with increasing pressure and their decrement is identical.

Fig. 13(i and j) show the predicted volume thermal expansion coefficient, α_V , as a function of the temperature and pressure of $\text{Ru}_4\text{Al}_3\text{B}_2$ and $\text{Ru}_9\text{Al}_3\text{B}_8$. Since $\text{Ru}_4\text{Al}_3\text{B}_2$ is less dense than $\text{Ru}_9\text{Al}_3\text{B}_8$, α_V is found to be higher in $\text{Ru}_4\text{Al}_3\text{B}_2$. α_V increases rapidly, especially up to $T < 300$ K, and then, it increases at a low pace in higher temperature regions. For both compounds, α_V follows the same pattern albeit with a discrepancy in their values. As pressure is increased, α_V falls exponentially. The higher value of α_V for $\text{Ru}_4\text{Al}_3\text{B}_2$ indicates that it is more ductile.

In a solid, the internal energy is the result of the random movement of molecules. Fig. 13(k and l) display the internal energy of the compounds as a function of temperature and pressure, respectively. U grows slowly in the low-temperature



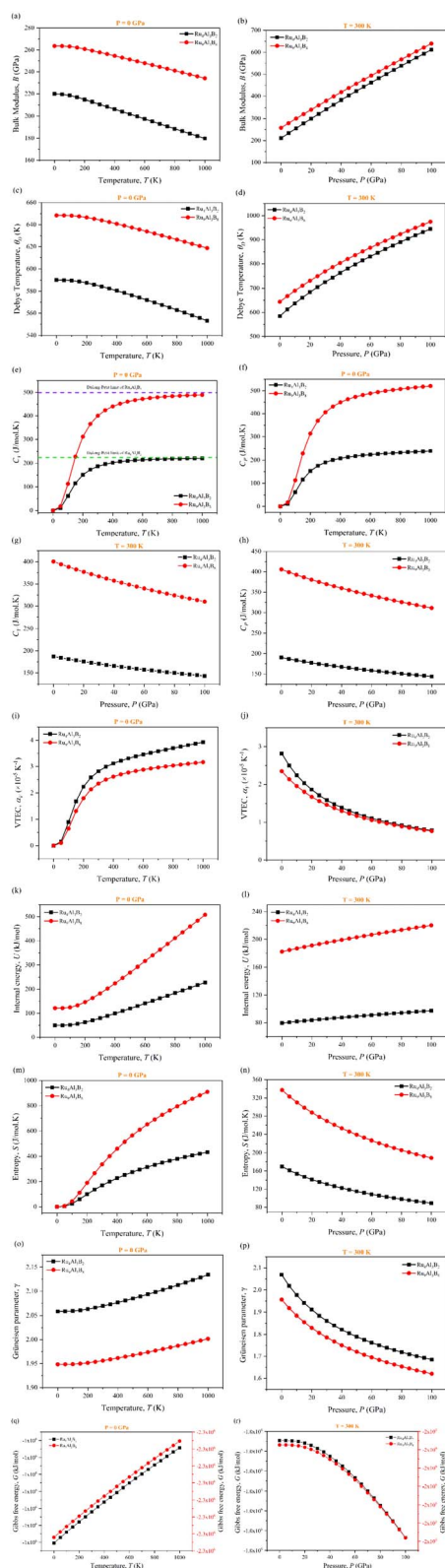


Fig. 13 Temperature and pressure dependence of (a–r) bulk modulus (B), Debye temperature (Θ_D), specific heat at constant pressure (C_P) and volume (C_V), volume expansion coefficient (α_V), internal energy (U), entropy (S), Grüneisen parameter (γ), and Gibbs's free energy (G) of $\text{Ru}_4\text{Al}_3\text{B}_2$ and $\text{Ru}_9\text{Al}_3\text{B}_8$.

region, but after $T > 200$ K, it increases more rapidly. Both the value and increase of the internal energy are greater for $\text{Ru}_9\text{Al}_3\text{B}_8$. Furthermore, from Fig. 13(l), it is observed that U increases in a linear pattern with increasing pressure at room temperature.

Entropy, S is a unit of measurement for how much a process causes the energy of atoms and molecules to disperse. The entropy variations of $\text{Ru}_4\text{Al}_3\text{B}_2$ and $\text{Ru}_9\text{Al}_3\text{B}_8$ as a function of temperature and pressure are depicted in Fig. 13(m and n). For low temperatures ($T < 100$ K), the value of entropy is almost the same for both compounds. In high temperature region ($T > 100$ K), the increase of entropy is very high for $\text{Ru}_9\text{Al}_3\text{B}_8$, and when 1000 K is reached, entropy in $\text{Ru}_9\text{Al}_3\text{B}_8$ is almost double compared to that in $\text{Ru}_4\text{Al}_3\text{B}_2$. It is also found that the entropy, S decreases with increasing pressure. This is due to the fact that the volume decreases with increasing pressure. The rate of decrease of entropy, S with pressure is similar for the two compounds.

The Grüneisen parameter, γ , describes how the specific heat of a material changes in response to changes in volume or pressure, and is related to the anharmonicity of the interatomic potentials in the material. Fig. 13(o and p) depicts the temperature and pressure dependence on the Grüneisen parameter. From Fig. 13(o), it can be seen that γ increases with temperature with $\text{Ru}_4\text{Al}_3\text{B}_2$ having a much higher value. On the other hand, γ decreases exponentially with pressure for both compounds as can be seen from Fig. 13(p).

Temperature and pressure dependent Gibbs's free energy of $\text{Ru}_4\text{Al}_3\text{B}_2$ and $\text{Ru}_9\text{Al}_3\text{B}_8$ are depicted in Fig. 13(q and r). Two separate scales had to be used for the compounds because of the vast difference between the values of Gibbs's energy of the two compounds follows the same pattern when the temperature is increased. It increases linearly. But, when the pressure is increased beyond 20 GPa, G decreases exponentially for both compounds.

4. Conclusion

A detailed investigation of the structural, vibrational, electronic, mechanical, and thermal properties of the Ru-based compounds, $\text{Ru}_4\text{Al}_3\text{B}_2$ and $\text{Ru}_9\text{Al}_3\text{B}_8$, was conducted using DFT method. The study found that both compounds are stable against decomposition into binary elements, as suggested by enthalpy calculations on phase stability. The phonon dispersion and density of states indicate that both compounds are dynamically stable, with no imaginary frequency observed in the phonon dispersion curves. The metallic character is confirmed by their electronic band structures. Both electron and hole like sheets are present in the Fermi surface. Both ionic and covalent bond characters are observed from Mulliken bond analysis and charge density profile. The stiffness constants, B , G , Y , H_{macro} , and H_{micro} of $\text{Ru}_9\text{Al}_3\text{B}_8$ were found to be higher than those of $\text{Ru}_4\text{Al}_3\text{B}_2$ implying that $\text{Ru}_9\text{Al}_3\text{B}_8$ is harder than the latter one. $\text{Ru}_4\text{Al}_3\text{B}_2$ possesses more elastic anisotropy than $\text{Ru}_9\text{Al}_3\text{B}_8$. For both compounds, various thermal properties, such as sound velocities, the Grüneisen parameter (γ), Debye and melting temperature (Θ_D , T_{min}), heat capacities (C_P , C_V),

volume thermal expansion coefficient (VTEC), and minimum and lattice thermal conductivity (k_{\min} , k_{ph}) were also calculated for different pressures. All the mechanical and thermodynamic properties are strongly depend on pressure and temperature. Therefore, the compounds are quite likely to come up with applied under high pressure and temperature environments. The optical absorption and photoconductivity spectra showed that both compounds exhibit metallic characteristics, and $\text{Ru}_9\text{Al}_3\text{B}_8$ was found to be better suited for potential applications as a thermal barrier coating (TBC) and solar absorber material for UV-based optical devices. We hope this work will inspire other research groups to investigate these exciting compounds in the near future.

Data availability

Data will be made available on request.

Conflicts of interest

The authors declare that they have no known competing financial interests or personal relationships that could have appeared to influence the work reported in this paper.

Acknowledgements

We acknowledge the Department of Physics, University of Rajshahi, Bangladesh for providing high configuration computing facilities.

References

- 1 M. Rajagopalan and M. Sundareswari, Ab initio study of the electronic structure of rhodium based intermetallic compounds under pressure, *J. Alloys Compd.*, 2004, **379**, 8–15, DOI: [10.1016/j.jallcom.2004.02.011](#).
- 2 J. Liang, D. Fan, P. Jiang, H. Liu and W. Zhao, First-principles study of the thermoelectric properties of intermetallic compound YbAl_3 , *Intermetallics*, 2017, **87**, 27–30.
- 3 T. An and F. Qin, Relationship between the intermetallic compounds growth and the microcracking behavior of lead-free solder joints, *J. Electron. Packag.*, 2016, **138**, 011002.
- 4 Y. Terada, K. Ohkubo, S. Miura, J. M. Sanchez and T. Mohri, Thermal conductivity and thermal expansion of L_{12} intermetallic compounds based on rhodium, *J. Alloys Compd.*, 2003, **354**, 202–207.
- 5 L. Mohammedi, B. Daoudi and A. Boukaraa, Ab-initio structural and electronic properties of the intermetallic compound TiFeH_2 , *Comput. Condens. Matter*, 2015, **2**, 11–15.
- 6 S. Murarka, *Metallization: Theory and Practice for VLSI and ULSI*, Butterworth-Heinemann, Boston, 1992.
- 7 J. Magnien, G. Khatibi, M. Lederer and H. Ipser, Investigation of interfacial behavior in miniaturized solder interconnects, *Mater. Sci. Eng., A*, 2016, **673**, 541–550.
- 8 K. S. Kim, S. H. Huh and K. Sukanuma, Effects of intermetallic compounds on properties of Sn–Ag–Cu lead-free soldered joints, *J. Alloys Compd.*, 2003, **352**, 226–236.
- 9 M. I. Naher, F. Parvin, A. K. M. A. Islam and S. H. Naqib, Physical properties of niobium-based intermetallics (Nb_3B ; B = Os, Pt, Au): a DFT-based ab initio study, *Eur. Phys. J. B*, 2018, **91**, 289, DOI: [10.1140/epjb/e2018-90388-9](#).
- 10 Y. Koo, S. Oh, K. Im and J. Kim, Ultrasonic spray pyrolysis synthesis of nano-cluster ruthenium on molybdenum dioxide for hydrogen evolution reaction, *Appl. Surf. Sci.*, 2023, **611**, 155774, DOI: [10.1016/j.apsusc.2022.155774](#).
- 11 W. Donphai, N. Thepphankulngarm, T. Chaisuwan, D. Tanangteerapong, S. C. Rood and P. Kongkachuichay, Catalytic performance of copper and ruthenium loaded on N-doped modified PBZ-derived carbons for CO_2 hydrogenation, *Chem. Eng. Sci.*, 2023, **274**, 118693, DOI: [10.1016/j.ces.2023.118693](#).
- 12 D. Majumdar, T. Maiyalagan and Z. Jiang, Recent Progress in Ruthenium Oxide-Based Composites for Supercapacitor Applications, *ChemElectroChem*, 2019, **6**, 4343–4372, DOI: [10.1002/celec.201900668](#).
- 13 E. Villemin, Y. C. Ong, C. M. Thomas and G. Gasser, Polymer encapsulation of ruthenium complexes for biological and medicinal applications, *Nat. Rev. Chem*, 2019, **3**, 261–282, DOI: [10.1038/s41570-019-0088-0](#).
- 14 R. Kumar and R. Thangappan, Electrode material based on reduced graphene oxide (rGO)/transition metal oxide composites for supercapacitor applications: a review, *Emergent Mater.*, 2022, **5**, 1881–1897, DOI: [10.1007/s42247-021-00339-7](#).
- 15 M. N. Hossain, S. Chen and A. Chen, Fabrication and electrochemical study of ruthenium-ruthenium oxide/activated carbon nanocomposites for enhanced energy storage, *J. Alloys Compd.*, 2018, **751**, 138–147, DOI: [10.1016/j.jallcom.2018.04.104](#).
- 16 S. K. Singh and D. S. Pandey, Multifaceted half-sandwich arene–ruthenium complexes: interactions with biomolecules, photoactivation, and multinuclearity approach, *RSC Adv.*, 2013, **4**, 1819–1840, DOI: [10.1039/C3RA44131H](#).
- 17 A. K. Sahu, D. K. Dash, K. Mishra, S. P. Mishra, R. Yadav, P. Kashyap, A. K. Sahu, D. K. Dash, K. Mishra, S. P. Mishra, R. Yadav, and P. Kashyap, *Properties and Applications of Ruthenium*, IntechOpen, 2018. DOI: [10.5772/intechopen.76393](#).
- 18 J. Liu, H. Lai, Z. Xiong, B. Chen and T. Chen, Functionalization and cancer-targeting design of ruthenium complexes for precise cancer therapy, *Chem. Commun.*, 2019, **55**, 9904–9914, DOI: [10.1039/C9CC04098F](#).
- 19 I. Zuba, M. Zuba, M. Piotrowski and A. Pawlukoć, Ruthenium as an important element in nuclear energy and cancer treatment, *Appl. Radiat. Isot.*, 2020, **162**, 109176, DOI: [10.1016/j.apradiso.2020.109176](#).
- 20 K. Lin, Z.-Z. Zhao, H.-B. Bo, X.-J. Hao and J.-Q. Wang, Applications of Ruthenium Complex in Tumor Diagnosis and Therapy, *Front. Pharmacol.*, 2018, **9**, 1323, DOI: [10.3389/fphar.2018.01323](#).
- 21 G. Sava and A. Bergamo, Ruthenium Drugs for Cancer Chemotherapy: An Ongoing Challenge to Treat Solid Tumours, in *Platin. Heavy Met. Compd. Cancer Chemother.*



- Mol. Mech. Clin. Appl.*, ed. A. Bonetti, R. Leone, F. M. Muggia, and S. B. Howell, Humana Press, Totowa, NJ, 2009, pp. 57–66, DOI: [10.1007/978-1-60327-459-3_8](#).
- 22 S. Hirt, F. Hilfinger and H. Hillebrecht, Synthesis and crystal structures of the new ternary borides $\text{Fe}_3\text{Al}_2\text{B}_2$ and $\text{Ru}_9\text{Al}_3\text{B}_8$ and the confirmation of $\text{Ru}_4\text{Al}_3\text{B}_2$ and $\text{Ru}_9\text{Al}_5\text{B}_{8-x}$ ($x \approx 2$), *Z. Kristallogr. – Cryst. Mater.*, 2018, **233**, 295–307, DOI: [10.1515/zkri-2017-2095](#).
 - 23 R. G. Parr, Density Functional Theory, *Annu. Rev. Phys. Chem.*, 1983, **34**, 631–656, DOI: [10.1146/annurev.pc.34.100183.003215](#).
 - 24 M. D. Segall, P. J. D. Lindan, M. J. Probert, C. J. Pickard, P. J. Hasnip, S. J. Clark and M. C. Payne, First-principles simulation: ideas, illustrations and the CASTEP code, *J. Phys.: Condens. Matter*, 2002, **14**, 2717–2744, DOI: [10.1088/0953-8984/14/11/301](#).
 - 25 D. Vanderbilt, Soft self-consistent pseudopotentials in a generalized eigenvalue formalism, *Phys. Rev. B: Condens. Matter Mater. Phys.*, 1990, **41**, 7892–7895, DOI: [10.1103/PhysRevB.41.7892](#).
 - 26 T. H. Fischer and J. Almlof, General methods for geometry and wave function optimization, *J. Phys. Chem.*, 1992, **96**, 9768–9774, DOI: [10.1021/j100203a036](#).
 - 27 S. Baroni, S. de Gironcoli, A. Dal Corso and P. Giannozzi, Phonons and related crystal properties from density-functional perturbation theory, *Rev. Mod. Phys.*, 2001, **73**, 515–562, DOI: [10.1103/RevModPhys.73.515](#).
 - 28 N. W. Ashcroft and N. D. Mermin, *Solid State Physics*, Holt-Saunders, 1976.
 - 29 A. Otero-de-la-Roza and V. Luaña, Gibbs2: A new version of the quasi-harmonic model code. I. Robust treatment of the static data, *Comput. Phys. Commun.*, 2011, **182**, 1708–1720, DOI: [10.1016/j.cpc.2011.04.016](#).
 - 30 A. Otero-de-la-Roza, D. Abbasi-Pérez and V. Luaña, Gibbs2: A new version of the quasiharmonic model code. II. Models for solid-state thermodynamics, features and implementation, *Comput. Phys. Commun.*, 2011, **182**, 2232–2248, DOI: [10.1016/j.cpc.2011.05.009](#).
 - 31 A. Chakraborty, M. N. H. Liton, M. S. I. Sarker, M. M. Rahman and M. K. R. Khan, A comprehensive DFT evaluation of catalytic and optoelectronic properties of BaTiO_3 polymorphs, *Phys. B*, 2023, **648**, 414418, DOI: [10.1016/j.physb.2022.414418](#).
 - 32 M. N. H. Liton, M. A. Helal, M. K. R. Khan, M. Kamruzzaman and A. K. M. Farid Ul Islam, Mechanical and opto-electronic properties of $\alpha\text{-MoSi}_2$: a DFT scheme with hydrostatic pressure, *Indian J. Phys.*, 2022, **96**, 4155–4172, DOI: [10.1007/s12648-022-02355-7](#).
 - 33 P. Li, G. Gao, Y. Wang and Y. Ma, Crystal Structures and Exotic Behavior of Magnesium under Pressure, *J. Phys. Chem. C*, 2010, **114**, 21745–21749, DOI: [10.1021/jp108136r](#).
 - 34 M. A. Omar, Elementary solid state physics: principles and applications, *Am. J. Phys.*, 1975, **43**, 929–933, DOI: [10.1119/1.9980](#).
 - 35 K. Refson, P. R. Tulip and S. J. Clark, Variational density-functional perturbation theory for dielectrics and lattice dynamics, *Phys. Rev. B: Condens. Matter Mater. Phys.*, 2006, **73**, 155114, DOI: [10.1103/PhysRevB.73.155114](#).
 - 36 G. Kresse, J. Furthmüller and J. Hafner, Ab initio force constant approach to phonon dispersion relations of diamond and graphite, *Europhys. Lett.*, 1995, **32**, 729.
 - 37 K. Parlinski, Z. Q. Li and Y. Kawazoe, First-principles determination of the soft mode in cubic ZrO_2 , *Phys. Rev. Lett.*, 1997, **78**, 4063.
 - 38 L. Lindsay, D. A. Broido and T. L. Reinecke, Thermal Conductivity and Large Isotope Effect in GaN from First Principles, *Phys. Rev. Lett.*, 2012, **109**, 095901, DOI: [10.1103/PhysRevLett.109.095901](#).
 - 39 J. F. Berry and C. C. Lu, Metal–Metal Bonds: From Fundamentals to Applications, *Inorg. Chem.*, 2017, **56**, 7577–7581, DOI: [10.1021/acs.inorgchem.7b01330](#).
 - 40 F. Mouhat and F.-X. Coudert, Necessary and sufficient elastic stability conditions in various crystal systems, *Phys. Rev. B: Condens. Matter Mater. Phys.*, 2014, **90**, 224104, DOI: [10.1103/PhysRevB.90.224104](#).
 - 41 M. E. Eberhart and T. E. Jones, Cauchy pressure and the generalized bonding model for nonmagnetic bcc transition metals, *Phys. Rev. B: Condens. Matter Mater. Phys.*, 2012, **86**, 134106, DOI: [10.1103/PhysRevB.86.134106](#).
 - 42 W. Feng and S. Cui, Mechanical and electronic properties of Ti_2AlN and Ti_4AlN_3 : a first-principles study, *Can. J. Phys.*, 2014, **92**, 1652–1657, DOI: [10.1139/cjp-2013-0746](#).
 - 43 W. Voigt, *Lehrbuch der Kristallphysik (mit Ausschluss der Kristalloptik)*, Vieweg+Teubner Verlag, 1966, DOI: [10.1007/978-3-663-15884-4](#).
 - 44 A. Reuss, Berechnung der Fließgrenze von Mischkristallen auf Grund der Plastizitätsbedingung für Einkristalle, *Z. Angew. Math. Mech.*, 1929, **9**, 49–58, DOI: [10.1002/zamm.19290090104](#).
 - 45 R. Hill, The Elastic Behaviour of a Crystalline Aggregate, *Proc. Phys. Soc., London, Sect. A*, 1952, **65**, 349–354, DOI: [10.1088/0370-1298/65/5/307](#).
 - 46 R. Hill, Elastic properties of reinforced solids: Some theoretical principles, *J. Mech. Phys. Solids*, 1963, **11**, 357–372, DOI: [10.1016/0022-5096\(63\)90036-X](#).
 - 47 M. Jamal, S. Jalali Asadabadi, I. Ahmad and H. A. Rahnamaye Aliabad, Elastic constants of cubic crystals, *Comput. Mater. Sci.*, 2014, **95**, 592–599, DOI: [10.1016/j.commatsci.2014.08.027](#).
 - 48 M. N. H. Liton, M. Roknuzzaman, M. A. Helal, M. Kamruzzaman, A. K. M. F. U. Islam, K. Ostrikov and M. K. R. Khan, Electronic, mechanical, optical and photocatalytic properties of perovskite $\text{RbSr}_2\text{Nb}_3\text{O}_{10}$ compound, *J. Alloys Compd.*, 2021, **867**, 159077, DOI: [10.1016/j.jallcom.2021.159077](#).
 - 49 M. N. H. Liton, M. A. Helal, A. K. M. Farid Ul Islam, M. Kamruzzaman, M. S. I. Sarker and M. K. R. Khan, Anisotropic elastic, opto-electronic and photocatalytic properties of BaTi_2O_5 : first-principles calculations, *Mater. Sci. Eng., B*, 2023, **296**, 116658, DOI: [10.1016/j.mseb.2023.116658](#).



- 50 W. Kim, Strategies for engineering phonon transport in thermoelectrics, *J. Mater. Chem. C*, 2015, **3**, 10336–10348, DOI: [10.1039/C5TC01670C](https://doi.org/10.1039/C5TC01670C).
- 51 I. N. Frantsevich, F. F. Voronov and S. A. Bakuta, *Handbook on Elastic Constants and Moduli of Elasticity for Metals and Nonmetals*, Naukova Dumka, Kiev, 1982.
- 52 Y. Cao, J. Zhu, Y. Liu, Z. Nong and Z. Lai, First-principles studies of the structural, elastic, electronic and thermal properties of Ni₃Si, *Comput. Mater. Sci.*, 2013, **69**, 40–45, DOI: [10.1016/j.commatsci.2012.11.037](https://doi.org/10.1016/j.commatsci.2012.11.037).
- 53 B. G. Pfrommer, M. Côté, S. G. Louie and M. L. Cohen, Relaxation of Crystals with the Quasi-Newton Method, *J. Comput. Phys.*, 1997, **131**, 233–240, DOI: [10.1006/jcph.1996.5612](https://doi.org/10.1006/jcph.1996.5612).
- 54 O. L. Anderson and H. H. Demarest Jr, Elastic constants of the central force model for cubic structures: Polycrystalline aggregates and instabilities, *J. Geophys. Res.*, 1971, **76**, 1349–1369, DOI: [10.1029/JB076i005p01349](https://doi.org/10.1029/JB076i005p01349).
- 55 Z. Sun, D. Music, R. Ahuja and J. M. Schneider, Theoretical investigation of the bonding and elastic properties of nanolayered ternary nitrides, *Phys. Rev. B: Condens. Matter Mater. Phys.*, 2005, **71**, 193402, DOI: [10.1103/PhysRevB.71.193402](https://doi.org/10.1103/PhysRevB.71.193402).
- 56 X.-Q. Chen, H. Niu, D. Li and Y. Li, Modeling hardness of polycrystalline materials and bulk metallic glasses, *Intermetallics*, 2011, **19**, 1275–1281, DOI: [10.1016/j.intermet.2011.03.026](https://doi.org/10.1016/j.intermet.2011.03.026).
- 57 A. Bouhemadou, First-principles study of structural, electronic and elastic properties of Nb₄AlC₃, *Braz. J. Phys.*, 2010, **40**, 52–57, DOI: [10.1590/S0103-97332010000100009](https://doi.org/10.1590/S0103-97332010000100009).
- 58 H. Niu, S. Niu and A. R. Oganov, Simple and accurate model of fracture toughness of solids, *J. Appl. Phys.*, 2019, **125**, 065105, DOI: [10.1063/1.5066311](https://doi.org/10.1063/1.5066311).
- 59 P. Ravindran, L. Fast, P. A. Korzhavyi, B. Johansson, J. Wills and O. Eriksson, Density functional theory for calculation of elastic properties of orthorhombic crystals: Application to TiSi₂, *J. Appl. Phys.*, 1998, **84**, 4891–4904, DOI: [10.1063/1.368733](https://doi.org/10.1063/1.368733).
- 60 H.-Y. Yan, M.-G. Zhang, D.-H. Huang and Q. Wei, First-principles study of elastic and thermodynamic properties of orthorhombic OsB₄ under high pressure, *Solid State Sci.*, 2013, **18**, 17–23, DOI: [10.1016/j.solidstatesciences.2012.12.015](https://doi.org/10.1016/j.solidstatesciences.2012.12.015).
- 61 A. K. M. F. U. Islam, M. N. H. Liton, H. M. T. Islam, M. A. Helal and M. Kamruzzaman, Mechanical and thermodynamical stability of BiVO₄ polymorphs using first-principles study, *Chin. Phys. B*, 2017, **26**, 36301–036301, DOI: [10.1088/1674-1056/26/3/036301](https://doi.org/10.1088/1674-1056/26/3/036301).
- 62 E. Schreiber, *Elastic Constants and Their Measurement*, McGraw-Hill Book Company, New York, 1973, http://181.176.223.4/opac_css/index.php?lvl=notice_display&id=6480.
- 63 D. L. Schodek, P. Ferreira and M. F. Ashby, *Nanomaterials, Nanotechnologies and Design: An Introduction for Engineers and Architects*, Butterworth-Heinemann, 2009.
- 64 O. L. Anderson, A simplified method for calculating the debye temperature from elastic constants, *J. Phys. Chem. Solids*, 1963, **24**, 909–917, DOI: [10.1016/0022-3697\(63\)90067-2](https://doi.org/10.1016/0022-3697(63)90067-2).
- 65 M. E. Fine, L. D. Brown and H. L. Marcus, Elastic constants versus melting temperature in metals, *Scr. Metall.*, 1984, **18**, 951–956, DOI: [10.1016/0036-9748\(84\)90267-9](https://doi.org/10.1016/0036-9748(84)90267-9).
- 66 D. R. Clarke, Materials selection guidelines for low thermal conductivity thermal barrier coatings, *Surf. Coat. Technol.*, 2003, **163–164**, 67–74, DOI: [10.1016/S0257-8972\(02\)00593-5](https://doi.org/10.1016/S0257-8972(02)00593-5).
- 67 D. S. Sanditov and V. N. Belomestnykh, Relation between the parameters of the elasticity theory and averaged bulk modulus of solids, *Tech. Phys.*, 2011, **56**, 1619–1623, DOI: [10.1134/S106378421111020X](https://doi.org/10.1134/S106378421111020X).
- 68 C. L. Wan, W. Pan, Q. Xu, Y. X. Qin, J. D. Wang, Z. X. Qu and M. H. Fang, Effect of point defects on the thermal transport properties of (La_xGd_{1-x})₂Zr₂O₇: Experiment and theoretical model, *Phys. Rev. B: Condens. Matter Mater. Phys.*, 2006, **74**, 144109, DOI: [10.1103/PhysRevB.74.144109](https://doi.org/10.1103/PhysRevB.74.144109).
- 69 Y. Liu, X. Zhao, Z. Yang, Z. Wang, X. Chen, S. Yang and M. Wei, New insights into element migration on La_{0.6}Sr_{0.4}Co_{0.2}Fe_{0.8}O_{3-δ} cathodes of intermediate temperature solid oxide fuel cells, *Solid State Ionics*, 2019, **334**, 145–151, DOI: [10.1016/j.ssi.2019.02.011](https://doi.org/10.1016/j.ssi.2019.02.011).
- 70 D. T. Morelli and G. A. Slack, High Lattice Thermal Conductivity Solids, in *High Therm. Conduct. Mater.*, ed. S. L. Shindé and J. S. Goela, Springer, New York, NY, 2006, pp. 37–68, DOI: [10.1007/0-387-25100-6_2](https://doi.org/10.1007/0-387-25100-6_2).
- 71 C. L. Julian, Theory of Heat Conduction in Rare-Gas Crystals, *Phys. Rev.*, 1965, **137**, A128–A137, DOI: [10.1103/PhysRev.137.A128](https://doi.org/10.1103/PhysRev.137.A128).
- 72 M. M. Ali, M. A. Hadi, M. L. Rahman, F. H. Haque, A. F. M. Y. Haider and M. Aftabuzzaman, DFT investigations into the physical properties of a MAB phase Cr₄AlB₄, *J. Alloys Compd.*, 2020, **821**, 153547, DOI: [10.1016/j.jallcom.2019.153547](https://doi.org/10.1016/j.jallcom.2019.153547).
- 73 M. W. Qureshi, M. A. Ali and X. Ma, Screen the thermomechanical and optical properties of the new ductile 314 MAX phase boride Zr₃CdB₄: A DFT insight, *J. Alloys Compd.*, 2021, **877**, 160248, DOI: [10.1016/j.jallcom.2021.160248](https://doi.org/10.1016/j.jallcom.2021.160248).
- 74 F. Parvin and S. H. Naqib, Pressure dependence of structural, elastic, electronic, thermodynamic, and optical properties of van der Waals-type NaSn₂P₂ pnictide superconductor: Insights from DFT study, *Results Phys.*, 2021, **21**, 103848, DOI: [10.1016/j.rinp.2021.103848](https://doi.org/10.1016/j.rinp.2021.103848).

